

Banner appropriate to article type will appear here in typeset article

# Capillary hysteresis induced by gap-resolved meniscus dynamics on Faraday instability in Hele-Shaw cells

Xingsheng Li<sup>1</sup>, Jing Li<sup>1</sup> and Xiaochen Li<sup>2</sup>

<sup>1</sup>Marine Numerical Experimental Center, State Key Laboratory of Ocean Engineering, School of Ocean and Civil Engineering, Shanghai Jiao Tong University, Shanghai, 200240, PR China

<sup>2</sup>School of Civil Engineering and Transportation, South China University of Technology, Guangzhou, 510630, PR China

**Corresponding author:** Jing Li, [lijing\\_@sjtu.edu.cn](mailto:lijing_@sjtu.edu.cn)

(Received xx; revised xx; accepted xx)

Existing theoretical analyses on Faraday waves in Hele-Shaw cells typically adopt gap-averaged governing equations and rely on Hamraoui's model coming from molecular kinetics theory, thereby oversimplifying essential transverse information, such as contact line velocity and capillary hysteresis, and conflicting with the unsteady meniscus dynamics. In this paper, a gap-resolved approach is developed by directly modeling the transverse gap flow and the contact angle dynamics, which overcomes the aforementioned limitations, ultimately yielding a modified damping with respect to the static contact angle and hysteresis range. A novel amplitude equation for Faraday waves is derived that combines this damping and the gap-averaged counterpart based on the oscillatory Stokes boundary layer, with the viscous dissipation preserved. By means of Lyapunov's first method, an explicit analytical expression for the critical stability boundary is established. Two series of laboratory experiments are performed that focus, respectively, on evolutions of the lateral meniscus and the longitudinal free surface near the Faraday onset, from which key parameters relevant to the theory are precisely measured. Based on the experimental data, the validity of the proposed mathematical model for addressing the Faraday instability problem in Hele-Shaw cells is confirmed, and the generation and development mechanisms of the onset are clarified. We find that the dispersion relation is significantly affected by the pinned contact line constraints, which partially compensate for the detuning caused by oscillatory Stokes flow approximation.

**Key words:** The authors should not enter keywords in the manuscript.

## 1. Introduction

Faraday waves, a typical resonant phenomenon in parametric excitation systems, appear on the free surface of fluid when the container is subjected to periodic vertical vibration with sufficient amplitude and frequency. Since first reported by Faraday (1831), advances in Faraday waves have proven to be fundamental for extensive scientific and industrial applications, including microscale assembly directed by liquid surface patterns (Chen *et al.* 2014), inkjet printing and deposition techniques (Arnold *et al.* 2007; Turkoz *et al.* 2019), atomization (Liu *et al.* 2019), and sloshing mitigation in aerospace and marine systems (Faltinsen 2017; Colville *et al.* 2025). These diverse applications have motivated numerous investigations into the underlying dynamics using experimental, theoretical, and numerical approaches (Benjamin & Ursell 1954; Müller 1993; Edwards & Fauve 1994; Kumar & Tuckerman 1994; Zhang & Viñals 1997; Périnet *et al.* 2009; Shao *et al.* 2021a).

Recent experiments in Hele-Shaw cells have significantly enriched the knowledge of Faraday waves, revealing new insights into confined interfacial instabilities. Rajchenbach *et al.* (2011) identified two novel classes of standing solitary waves of large amplitude, distinguished by odd and even symmetries. Inspired by this pioneering work, a system of two coupled Faraday waves was observed at the two interfaces of three layers of fluids (Li *et al.* 2018b). Furthermore, steady streaming patterns and self-organization of small tracers sustained by longitudinal Faraday waves were observed in narrow rectangular containers, though not strictly sorted into Hele-Shaw cells (Périnet *et al.* 2017; Alarcón *et al.* 2020). These novel findings indicate that Faraday waves in tanks with a narrow gap exhibit more complicated dynamics than those in wide-mouth containers, with the governing mechanisms remaining incompletely understood.

Existing theoretical and numerical frameworks have focused predominantly on Faraday waves with spatially regular profiles, as observed by Pradenas *et al.* (2017) and Li *et al.* (2019b) in Hele-Shaw experiments. What researchers interest are the critical condition for the emergence of these stationary patterns that uniformly occupy the entire laboratory-scale cells, which is called the Faraday onset. Consistent with the parametric instability problem in wide-mouth containers (Benjamin & Ursell 1954; Kumar & Tuckerman 1994), linear stability analysis serves as a common method for characterizing the onset conditions in Hele-Shaw configurations. Current studies have pursued two distinct approaches: one is Floquet theory, which reduces to a generalized eigenvalue problem followed by a numerical solving process (Li *et al.* 2018a; Bongarzone *et al.* 2023); the other is Lyapunov's first method applied to the nonlinear dynamic system described by the amplitude equation, producing analytical expressions for the critical acceleration threshold (Rajchenbach *et al.* 2011; Li *et al.* 2019a). The amplitude equation for the complex amplitude  $A(t)$  has the form

$$\frac{dA}{dt} = (\alpha_1 + i\alpha_2) A + \alpha_3 A^* - i\alpha_4 |A|^2 A, \quad (1.1)$$

where  $\alpha_1$  characterizes system damping,  $\alpha_2$  corresponds to the natural-response frequency detuning,  $\alpha_3$  captures parametric forcing strength, and the last term is related to the nonlinear frequency shift with the wave amplitude. Despite methodological differences, all stability analysis methods reveal the decisive dependence of critical threshold on the damping coefficient  $\alpha_1$ , whose precise quantification has been a persistent challenge.

One of the dominant dissipation originates from the no-slip condition at two lateral walls. For sufficiently small gap sizes  $b$  (typically satisfying  $bk \ll 1$  according to Schwartz (1986), with  $k$  being the wavenumber), the transverse flow is strongly constrained. The inherent conflict between the no-slip boundary condition and vertical kinematics of Faraday waves makes it difficult to develop a fully three-dimensional mathematical model for

this system. Based on Darcy's law, Gondret & Rabaud (1997) developed an effective transverse averaging technique when studying the parallel flow driven by a given pressure gradient, which promotes the theoretical framework on the Faraday instability problem (Rajchenbach *et al.* 2011). The assumption of a Poiseuille flow profile in the gap direction yields a parabolic velocity distribution that, when integrated and averaged, produces a characteristic damping coefficient  $12\nu/b^2$ , with  $\nu$  denoting the kinematic viscosity. Although Rajchenbach *et al.* (2011) incorporated this damping coefficient and proposed an amplitude equation that governs the dynamics of Faraday waves, their formulation is incomplete since the surface tension effects are entirely neglected. Li *et al.* (2018a) established the gap-averaged Navier-Stokes equations and implemented them in the open-source solver Gerris (Popinet 2003, 2009). While the two-dimensional Faraday wave patterns were successfully reproduced and flow information was obtained, the lack of any contact angle model impedes accurate calculation of the instability threshold. Li *et al.* (2019a) extended this theory by incorporating meniscus effects and modifying  $\alpha_1$  with dynamic contact angle damping based on Hamraoui's model, subsequently derived a new amplitude equation from the gap-averaged governing equations. By means of Lyapunov's first method, they obtained an explicit expression for the instability threshold that shows substantial improvement due to the inclusion of contact angle dynamics. However, systematic discrepancies between theory and experiment remain to be addressed.

Progress in this direction was recently made by Bongarzone *et al.* (2023). Although Darcy's law accurately models unidirectional steady flows, its applicability to Faraday instability problem is limited by the inability to capture convective and unsteady inertial effects in periodically oscillating systems. Inspired by the application of a classical Womersley velocity profile in pulsating flows in a channel (Womersley 1955; San & Staples 2012) and the foundational work on sloshing dynamics in Hele-Shaw cells (Viola *et al.* 2017), Bongarzone *et al.* (2023) proposed a revised gap-averaged Floquet analysis. The Poiseuille velocity profile was updated by the Womersley-like solution to Stokes boundary layer theory, resulting in a modified gap-averaged damping coefficient that accounts for oscillatory flow effects. Contact angle damping was taken into account with Hamraoui's model employed by Li *et al.* (2019a). Comparison with experiments confirms that their predictions of the instability threshold are remarkably improved, revealing that Darcy's law indeed underestimates the effective gap-averaged damping. Based on this oscillatory Stokes flow approximation, we have developed a fully viscous theory and found that bulk viscous dissipation plays a negligible role in linear stability analysis (Li & Li 2024), while Hamraoui's model was maintained when dealing with the dynamic contact angle. These analyses demonstrate that Stokes boundary layer theory yields a more accurate description of the gap flow. However, this transverse flow approximation also introduces an unexpected detuning, which was reported by Bongarzone *et al.* (2023), appearing as a characteristic shift in the response frequency. This can also be reflected in the dispersion relation. It should be noted that this anomalous detuning was not observed by Li *et al.* (2019a), implying that Hamraoui's dynamic contact angle model probably conflicts with the oscillatory Stokes boundary layer.

The effect of dynamic contact angle, which has been neglected in many literature (Rajchenbach *et al.* 2011; Pradenas *et al.* 2017; Li *et al.* 2018a; Rachik & Aniss 2023), was first taken into account by Li *et al.* (2019a) when deriving the amplitude equation, embracing a model proposed by Hamraoui *et al.* (2000):

$$\cos \theta = 1 - \frac{\beta}{\mu} Ca, \quad \text{with } Ca = \frac{\mu}{\sigma} w, \quad (1.2)$$

where  $\theta$  is the contact angle formed by the intersection of the free surface and the lateral wall at the contact line,  $\beta$  is a friction coefficient,  $\mu$  is dynamic viscosity,  $\sigma$  is surface tension coefficient, and  $Ca$  is the Capillary number defined by vertical velocity  $w$ . Although its applicability has been verified in many investigations (Bongarzone *et al.* 2023; Li & Li 2024), there are several critical limitations. First, this equation was originally developed for the kinetics of capillary rise, where the unidirectional flow feature guarantees mathematical rigor. When applied to periodically oscillating systems, (1.2) produces a nonphysical phenomenon ( $\cos \theta > 1$ ) for negative velocity ( $w < 0$ ). In other words, this formulation contradicts the unsteady Stokes flow. Second, existing theoretical analyses rely on the experimental values of  $\beta$  measured by Hamraoui *et al.* (2000), which were carried out in glass capillaries. According to Young's equation, the wettability is sensitive to the solid substrate (De Gennes 1985; Good 1992), implying that  $\beta$  necessarily depends on the container material characteristics, while previous work abused its measurements in different scenarios. Finally, (1.2) establishes a linear relationship between  $\cos \theta$  and  $w$ . The velocity  $w$  refers to the motion of the contact line but is estimated by the vertical velocity of the free surface. As will be demonstrated later in this paper, our laboratory observations indicate that before Faraday waves emerge, the contact line remains effectively pinned during initial excitation, while the contact angle varies within a specific range. This widely used model cannot capture contact angle variations under pinned contact line conditions, namely contact angle hysteresis effects.

Based on numerous established theories on contact line boundary conditions in free surface flows (Hocking 1987; Cocciaro *et al.* 1993; Ting & Perlin 1995; Jiang *et al.* 2004; Viola *et al.* 2018; Shao *et al.* 2021*b*), we aim at seeking a refined contact angle model that better captures the dynamics of meniscus. Since the contact angle should be determined locally on the lateral walls, exhibiting a behavior dominated by transverse meniscus dynamics, its dimension is orthogonal to the in-plane Faraday waves. Given the challenge of developing a complete three-dimensional mathematical model, we decompose the fluid domain into two distinct regions for separate analysis. On the one hand, we focus on the Faraday wave profile and neglect the meniscus effects. Following the approach taken by Li *et al.* (2019*a*), we derive the amplitude equation for Faraday waves based on the oscillatory Stokes flow assumption. Bulk viscous dissipation can be retained through the application of viscous flow theory. Specifically, we will demonstrate why the contact angle dynamics cannot be incorporated directly into the gap-averaged governing equations. On the other hand, we concentrate on the meniscus and try to directly resolve the transverse gap flow dynamics, which enables implementation of a more comprehensive contact angle hysteresis model and integration of contact angle damping into an amplitude equation. The gap-resolved approach can preserve essential transverse information oversimplified by existing frameworks. Then we verify the feasibility of incorporating the contact angle damping into the amplitude equation for Faraday waves. Thus, an amplitude equation formed as (1.1) can be established, followed by a linear stability analysis. Lastly, quantitative comparisons with experimental measurements are necessary to confirm the validity of the mathematical model. These efforts may contribute to reveal the generation mechanism of the onset and clarify the crucial role of pinned contact line effects in Faraday instability problem in Hele-Shaw cells.

The paper is organized as follows. In § 2, we derive the amplitude equation for Faraday waves based on the Stokes boundary layer theory and retain the bulk viscous dissipation. In § 3, we present a gap-resolved approach and derive the contact angle hysteresis damping. The experimental methodology is described in § 4, together with some comparisons to numerically solved meniscus dynamics. Linear stability analysis and theoretical model

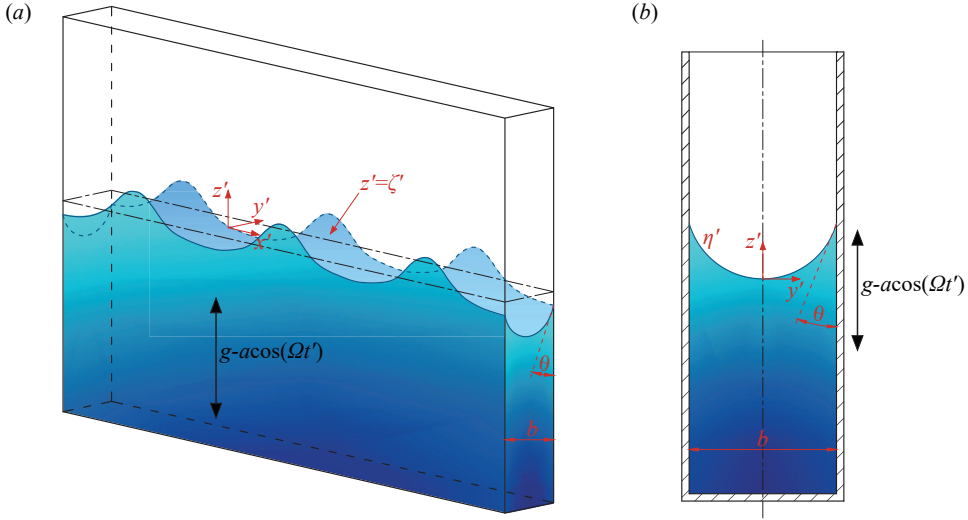


Figure 1. (a) Sketch of Faraday waves in a Hele-Shaw cell that undergoes a vertical sinusoidal oscillation of acceleration amplitude  $a$  and angular frequency  $\Omega$ . The free surface elevation denoted by  $\zeta'$  ( $x', y', t'$ ) contains both the two-dimensional Faraday wave profile along  $x'$ -direction and the meniscus in the gap direction. (b) View of the gap between two lateral walls. Here  $b$  denotes the gap size of the Hele-Shaw cell and  $\theta$  is the contact angle of the liquid on the lateral walls. The meniscus profile is denoted by  $\eta'$  ( $x', y', t'$ ).

validation are performed in § 5, where other detailed discussions are also reported. Finally, some conclusions are given in § 6.

## 2. Amplitude equation for Faraday waves

We consider here a horizontally infinite Hele-Shaw cell of width  $b$  filled with a kind of liquid of density  $\rho$  and dynamic viscosity  $\mu$  (kinematic viscosity  $\nu = \mu/\rho$ ). The container undergoes a vertical sinusoidal oscillation with acceleration amplitude  $a$  and angular frequency  $\Omega$ . In the Cartesian coordinate system as shown in figure 1 that moves with the oscillating container,  $z' = 0$  is set at the bottom of the meniscus when at rest. The central objective is to determine the critical condition for the onset of Faraday waves from an initially still free surface by stability analysis of the amplitude equation.

### 2.1. Mathematical model for instability problem

#### 2.1.1. Oscillatory Stokes flow

Stokes boundary layer theory has been effectively validated in characterizing the influence of two lateral walls in the Hele-Shaw flow (Viola *et al.* 2017; Bongarzone *et al.* 2023; Li & Li 2024). The primary procedure is to derive the velocity profile along the gap direction and then calculate its spatial average to quantify the damping induced by the lateral confinement.

Under vertical periodic vibration, the effective gravitational acceleration is given by  $G(t') = g - a \cos(\Omega t')$ . Linearizing the Navier-Stokes equations about the state of rest  $\mathbf{U}' = 0$  and  $P'(z', t') = -\rho G(t') z'$ , the equations for the perturbation fields of velocity,  $\mathbf{u}'(x', y', z', t') = (u', v', w')^T$ , and pressure,  $p'(x', y', z', t')$ , within the fluid bulk read

$$\frac{\partial \mathbf{u}'}{\partial t'} = -\frac{1}{\rho} \nabla' p' + \nu \nabla'^2 \mathbf{u}', \quad \nabla' \cdot \mathbf{u}' = 0. \quad (2.1)$$

According to the feature of Faraday waves in Hele-Shaw cells, the gap is narrow enough that  $bk \ll 1$  with  $k$  denoting the wavenumber. We assume that there are no flows along the  $y'$ -direction and the velocity satisfies  $v' = 0$ . Equations in (2.1) then reduce to

$$\frac{\partial u'}{\partial t'} = -\frac{1}{\rho} \frac{\partial p'}{\partial x'} + \nu \frac{\partial^2 u'}{\partial y'^2}, \quad \frac{\partial w'}{\partial t'} = -\frac{1}{\rho} \frac{\partial p'}{\partial x'} + \nu \frac{\partial^2 w'}{\partial y'^2}, \quad \frac{\partial p'}{\partial y'} = 0, \quad (2.2a)$$

$$\frac{\partial u'}{\partial x'} + \frac{\partial w'}{\partial z'} = 0. \quad (2.2b)$$

By making dimensionless with the following expressions:

$$\begin{aligned} x &= kx', \quad y = \frac{y'}{b}, \quad z = kz', \quad u = \frac{\Omega u'}{g}, \quad v = \frac{\Omega v'}{bkg}, \\ w &= \frac{\Omega w'}{g}, \quad p = \frac{kp'}{\rho g}, \quad t = \Omega t', \quad \zeta = k\zeta', \end{aligned} \quad (2.3a-i)$$

the first two equations in (2.2a) in dimensionless form become

$$\frac{\partial u}{\partial t} = -\frac{\partial p}{\partial x} + \frac{\delta_{St}^2}{2} \frac{\partial^2 u}{\partial y^2}, \quad \frac{\partial w}{\partial t} = -\frac{\partial p}{\partial z} + \frac{\delta_{St}^2}{2} \frac{\partial^2 w}{\partial y^2}, \quad (2.4a,b)$$

where  $\delta_{St} = \sqrt{2\nu/\Omega}/b$  is the dimensionless thickness of the oscillating Stokes boundary layer (Bongarzone *et al.* 2023).

Because Faraday waves observed in Hele-Shaw cell experiments possess a subharmonic oscillation at a frequency of  $\Omega/2$  (Li *et al.* 2019b), only the fundamental mode is considered, which is reflected in the separated exponential part of solutions associated with periodicity. Therefore, the ansatzes can be written as  $\mathbf{u}(x, y, z, t) = \text{Re} [\tilde{\mathbf{u}}(x, y, z) e^{it/2}]$  and  $p(x, z, t) = \text{Re} [\tilde{p}(x, z) e^{it/2}]$ . Substituting them into (2.4a,b), together with the no-slip condition at  $y = \pm 1/2$ , the resulting ordinary differential equations about  $y$  are solved. Then we have

$$\tilde{u} = 2i \left\{ 1 - \frac{\cosh[(1+i)y/\delta_1]}{\cosh[(1+i)/2\delta_1]} \right\} \frac{\partial \tilde{p}}{\partial x}, \quad \tilde{w} = 2i \left\{ 1 - \frac{\cosh[(1+i)y/\delta_1]}{\cosh[(1+i)/2\delta_1]} \right\} \frac{\partial \tilde{p}}{\partial z}, \quad (2.5a,b)$$

where  $\delta_1 = \delta_{St}/\sqrt{1/2}$  is a modified dimensionless Stokes boundary layer thickness specific to the fundamental wave mode.

By integrating (2.5a,b) along  $y'$ -direction and taking the average, the gap-averaged velocity components  $\bar{u}$  and  $\bar{w}$  are expressed by the two-dimensional pressure field  $\bar{p}$ , namely

$$\bar{u}(x, z, t) = \lambda_1 \frac{\partial \bar{p}}{\partial x}, \quad \bar{w}(x, z, t) = \lambda_1 \frac{\partial \bar{p}}{\partial z}, \quad (2.6a,b)$$

with

$$\lambda_1 = 2i \{ 1 - (1-i)\delta_1 \tanh[(1+i)/2\delta_1] \}. \quad (2.7)$$

After this gap-averaging process, the Hele-Shaw flow reduces to two-dimensional dynamics in the  $x'$ - $z'$  plane and the dissipation resulting from the lateral walls is implicitly incorporated in the coefficient  $\lambda_1$ .

### 2.1.2. Governing equations

The dimensionless continuity equation of (2.2b), when gap-averaged and combined with (2.6a,b), is simplified to a Laplace equation for the pressure field:

$$\frac{\partial^2 \bar{p}}{\partial x^2} + \frac{\partial^2 \bar{p}}{\partial z^2} = 0. \quad (2.8)$$

The dimensionless non-penetrable boundary condition at the solid bottom reads

$$\frac{\partial \bar{p}}{\partial z} = 0, \quad \text{at } z = -\infty. \quad (2.9)$$

Assuming that the location of the bottom extends to  $z = -\infty$  is feasible since the experimental liquid layer is sufficiently deep and  $kH \gg 1$  with  $H$  denoting the liquid depth.

On the moving free surface, the normal stress is balanced by capillary force. We mention here the Taylor expansion of boundary conditions on the free surface around  $z' = 0$  and, following eliminating the nonlinear terms, the normal stress boundary condition reads

$$-p' + \rho G(t') \zeta' + 2\mu \frac{\partial w'}{\partial z'} = \sigma \left( \frac{\partial^2 \zeta'}{\partial x'^2} + \frac{\partial^2 \zeta'}{\partial y'^2} \right), \quad \text{at } z' = 0, \quad (2.10)$$

where  $\sigma$  is the surface tension coefficient. The right-hand side of (2.10) represents the capillary force, incorporating curvature contributions from two principal directions. To characterize the constitution of the three-dimensional free surface (see the sketches in figure 1), we decompose it into two distinct components: the two-dimensional Faraday wave profile  $\bar{\zeta}'$  corresponding to the projection of the meniscus base onto  $x'$ - $z'$  plane, and the capillary driven meniscus  $\eta'$  in the narrow gap direction. The observed free surface deformation is a superposition of these two parts, namely

$$\zeta'(x', y', t') = \eta'(x', y', t') + \bar{\zeta}'(x', t'). \quad (2.11)$$

Typically, retaining  $\eta'$  in the derivation leads directly to contact angle damping. Because this damping will be addressed in the next section and only the Faraday wave profile is considered in the current analysis (that is, only  $\bar{\zeta}'$  is preserved in (2.11)), the meniscus curvature term  $\partial^2 \zeta' / \partial y'^2$  in (2.10) should be removed. After turning into dimensionless form using (2.3a-i) and gap-averaging in the  $y'$ -direction, the boundary condition (2.10) becomes

$$-\bar{p} + \left(1 - \frac{a}{g} \cos t\right) \bar{\zeta} + \delta_{St}^2 k^2 b^2 \lambda_1 \frac{\partial^2 \bar{p}}{\partial z^2} = l_c^2 k^2 \frac{\partial^2 \bar{\zeta}}{\partial x^2}, \quad \text{at } z = 0, \quad (2.12)$$

where  $l_c = \sqrt{\sigma/\rho g}$  denotes the capillary length, and  $\bar{\zeta}$  represents the gap-averaged two-dimensional Faraday wave profile that has been made dimensionless with  $\bar{\zeta} = k \bar{\zeta}'$ . In (2.12), the viscous stress reflected by the term  $\partial^2 \bar{p} / \partial z^2$  is retained. Although the previous theory indicates that the effect of fluid viscosity on dissipation in the Hele-Shaw system can be neglected (Li & Li 2024), and this viscous term, scaling as  $\delta_{St}^2 k^2 b^2 \ll 1$ , has been ignored by Li *et al.* (2019a) and Bongarzone *et al.* (2023), we retain it to preserve the fidelity of damping representation, with a detailed discussion on this viscous dissipation later.

The second boundary condition on the free surface is the linearized kinematic condition, whose dimensionless form is

$$\frac{\Omega^2}{gk} \frac{\partial \bar{\zeta}}{\partial t} = w, \quad \text{at } z = 0. \quad (2.13)$$

After gap-averaging, (2.13) reduces to

$$\frac{\Omega^2}{gk} \frac{\partial \bar{\zeta}}{\partial t} = \lambda_1 \frac{\partial \bar{p}}{\partial z}, \quad \text{at } z = 0. \quad (2.14)$$

The system of equations (2.8), (2.9), (2.12), and (2.14) constitutes the governing equations for the Faraday instability problem in Hele-Shaw cells under the oscillatory Stokes flow approximation.

## 2.2. Asymptotic expansion

The derivation of amplitude equations is a classical method to describe pattern selection beyond linear instability (see, for instance, the frameworks of Milner (1991), Chen & Vinals (1999), and Westra *et al.* (2003)). This approach is also applied to obtain the critical condition for linear stability of Faraday waves in Hele-Shaw cells (Rajchenbach *et al.* 2011; Li *et al.* 2019a). Inspired by these studies, we derive the amplitude equation from the reestablished mathematical model given in § 2.1.2.

By introducing an expansion parameter  $\epsilon$ , the physical parameters can be expressed by

$$a = \epsilon \hat{a}, \quad \delta_{St}^2 k^2 b^2 = \epsilon \hat{\delta}, \quad \lambda_1 = 2i(1 - \epsilon \hat{\delta}_1), \quad (2.15a-c)$$

where  $\epsilon \hat{\delta}_1 = (1 - i) \delta_1 \tanh[(1 + i)/2\delta_1]$  is the damping part of  $\lambda_1$ . To examine the variation of variables in a long time scale, in the spirit of multiple scale analysis (Nayfeh 1993), a slow time scale  $T = \epsilon t$  is introduced, and naturally  $\partial_t \rightarrow \partial_t + \epsilon \partial_T$ . Then the rescaled governing equations read

$$\frac{\partial^2 \bar{p}}{\partial x^2} + \frac{\partial^2 \bar{p}}{\partial z^2} = 0, \quad (2.16a)$$

$$-\bar{p} + \left(1 - \epsilon \frac{\hat{a}}{g} \cos t\right) \bar{\zeta} + \epsilon \hat{\delta} 2i(1 - \epsilon \hat{\delta}_1) \frac{\partial^2 \bar{p}}{\partial z^2} = l_c^2 k^2 \frac{\partial^2 \bar{\zeta}}{\partial x^2}, \quad \text{at } z = 0, \quad (2.16b)$$

$$4\omega^2 \left(1 + l_c^2 k^2\right) \left(\frac{\partial \bar{\zeta}}{\partial t} + \epsilon \frac{\partial \bar{\zeta}}{\partial T}\right) = 2i(1 - \epsilon \hat{\delta}_1) \frac{\partial \bar{p}}{\partial z}, \quad \text{at } z = 0, \quad (2.16c)$$

$$\frac{\partial \bar{p}}{\partial z} = 0, \quad \text{at } z = -\infty. \quad (2.16d)$$

In (2.16c), the angular frequency has been nondimensionalized with the expression  $\Omega/2 = \omega \sqrt{gk + \sigma k^3/\rho}$ . We shall define  $\omega_0$  the limit of response frequency  $\omega$  when  $\epsilon = 0$  with expansion  $\omega^2 = \omega_0^2 + \epsilon \omega_1^2$ . The variables in (2.16a)-(2.16d) are expanded as follows:

$$\bar{p} = \bar{p}_1 + \epsilon \bar{p}_2 + O(\epsilon^2), \quad \bar{\zeta} = \bar{\zeta}_1 + \epsilon \bar{\zeta}_2 + O(\epsilon^2). \quad (2.17a-b)$$

According to these definitions, we find that  $\bar{p} \sim O(1)$ ,  $\bar{\zeta} \sim O(1)$ ,  $a \sim O(\epsilon)$ ,  $\delta_{St}^2 k^2 b^2 \sim O(\epsilon)$ , and the damping part of  $\lambda_1$  is of the order  $\sim O(\epsilon)$ . Given  $\bar{\zeta} = 0$  and  $\bar{p} = 0$  in the absence of external forcing, the solutions corresponding to the static state are homogeneous. Hence, only the varying parts are retained in (2.17a-b).

For each order problem, (2.16a) and (2.16d) will not change, and thus only boundary conditions on the free surface are listed. At order  $\epsilon^0$ , (2.16b) and (2.16c) reduce to

$$-\bar{p}_1 + \bar{\zeta}_1 - l_c^2 k^2 \frac{\partial^2 \bar{\zeta}_1}{\partial x^2} = 0, \quad \text{at } z = 0, \quad (2.18a)$$



$$4\omega_0^2 \left(1 + l_c^2 k^2\right) \frac{\partial \bar{\xi}_1}{\partial t} - 2i \frac{\partial \bar{p}_1}{\partial z} = 0, \quad \text{at } z = 0. \quad (2.18b)$$

The solutions read

$$\bar{p}_1 = \left(1 + l_c^2 k^2\right) \cos x e^{iz} e^{it/2} A(T) + \text{c.c.}, \quad (2.19a)$$

$$\bar{\xi}_1 = \cos x e^{it/2} A(T) + \text{c.c.}, \quad (2.19b)$$

where  $\omega_0 = 1$  represents a traditional dispersion relation for gravity-capillary waves,  $A(T)$  is the complex amplitude, and c.c. denotes the complex conjugate.

At order  $\epsilon$ , (2.16b) and (2.16c) are written as

$$-\bar{p}_2 + \bar{\xi}_2 - l_c^2 k^2 \frac{\partial^2 \bar{\xi}_2}{\partial x^2} = \frac{\hat{a}}{g} \cos t \bar{\xi}_1 - 2i \delta \frac{\partial^2 \bar{p}_1}{\partial z^2}, \quad \text{at } z = 0, \quad (2.20a)$$

$$4 \left(1 + l_c^2 k^2\right) \frac{\partial \bar{\xi}_2}{\partial t} - 2i \frac{\partial \bar{p}_2}{\partial z} = -4 \left(1 + l_c^2 k^2\right) \frac{\partial \bar{\xi}_1}{\partial T} - 4\omega_1^2 \left(1 + l_c^2 k^2\right) \frac{\partial \bar{\xi}_1}{\partial t} - 2i \delta_1 \frac{\partial \bar{p}_1}{\partial z}, \quad \text{at } z = 0. \quad (2.20b)$$

By solving  $\bar{\xi}_2$  using (2.20b), and combining it with (2.20a), an equation of  $\bar{p}_2$  is obtained. Substituting (2.19a) and (2.19b) into this equation, according to the Fredholm alternative, a solvability condition appears on the right-hand side, which leads to

$$\frac{dA}{dT} + \frac{1}{2} \left[ i \left( \hat{\delta}_{1,r} + i \hat{\delta}_{1,i} \right) + i \omega_1^2 + 2\hat{\delta} \right] A + \frac{i \hat{a}}{4g \left(1 + l_c^2 k^2\right)} A^* = 0, \quad (2.21)$$

where  $\hat{\delta}_{1,r}$  and  $\hat{\delta}_{1,i}$  are the real and imaginary parts of  $\hat{\delta}_1$ , respectively, and the asterisk (\*) designates the complex conjugate.

Equation (2.21) is the amplitude equation for Faraday waves that incorporates dissipation from both the confinement of the lateral walls and viscous stress, but excludes capillary damping induced by contact angle dynamics. To derive an explicit expression of the damping, we decompose the complex amplitude  $A$  into modulus and phase and write the modulus as  $|A| = A_0 e^{-\gamma_1 t}$ . Thus, the damping rate  $\gamma_1$  is calculated by

$$\gamma_1 = -\frac{d \log(|A|/A_0)}{dt} = -\frac{\epsilon}{|A|} \frac{d|A|}{dT} = \frac{1}{2} \left[ i \left( \delta_{1,r} + i \delta_{1,i} \right) + i \left( \omega^2 - 1 \right) + 2\delta_{St}^2 k^2 b^2 \right], \quad (2.22)$$

where  $\delta_{1,r}$  and  $\delta_{1,i}$  denote the real and imaginary parts of  $(1 - i) \delta_1 \tanh[(1 + i)/2\delta_1]$ , respectively, and are associated with the gap-averaged damping. The last term  $\delta_{St}^2 k^2 b^2$  reflects the viscous dissipation arising from the normal stress boundary condition (2.10).

### 3. Contact angle hysteresis damping

Existing theories for Faraday waves in Hele-Shaw cells typically employ the gap-averaging strategy. Although the gap size  $b$  is rather small and the assumption  $kb \ll 1$  renders the instability problem nominally two-dimensional, the transverse meniscus determines the contact angle damping. In this section, we first extend the analysis presented in § 2 by incorporating meniscus effects, thereby demonstrating the limitation of Hamraoui's model (1.2) and the infeasibility of implementing a contact angle model in the gap-averaged governing equations. We then concentrate on the dynamics in the gap (see figure 1b) and develop a more rigorous formulation for contact angle hysteresis damping.

### 3.1. Incorporating meniscus effects into gap-averaged equations

If we take the meniscus  $\eta'$  into account and substitute (2.11) into (2.10), another gap-averaged normal stress boundary condition is obtained that

$$-\bar{p} + \left(1 - \frac{a}{g} \cos t\right) \bar{\zeta} + \delta_{St}^2 k^2 b^2 \lambda_1 \frac{\partial^2 \bar{p}}{\partial z^2} = l_c^2 \left( k^2 \frac{\partial^2 \bar{\zeta}}{\partial x^2} + \frac{2}{b^2} \frac{\partial \eta}{\partial y} \Big|_{y=1/2} \right), \quad \text{at } z = 0, \quad (3.1)$$

where  $\eta'$  has been nondimensionalized with  $\eta = k\eta'$ . Comparing with (2.12), the last term in (3.1) refers to the curvature in the  $y'$ -direction, and is associated with the contact angle  $\theta$  through the geometrical relation  $\partial \zeta' / \partial y' |_{y'=\pm b/2} = \pm \cot \theta$ , whose dimensionless form produces

$$\frac{\partial \eta}{\partial y} = \pm k b \cot \theta, \quad \text{at } y = \pm \frac{1}{2}. \quad (3.2)$$

Before the emergence of Faraday waves, the meniscus fluctuates up-and-down periodically and  $\theta$  changes constantly around a static contact angle  $\theta_s$ . Existing theoretical analyses typically use the dynamic contact angle model (1.2) developed by Hamraoui *et al.* (2000) to define the variation of the dynamic contact angle with vertical velocity (Li *et al.* 2019a; Bongarzone *et al.* 2023; Li & Li 2024). Figure 2a shows the dependence of  $\theta$  on  $Ca$  as defined by (1.2), namely  $\theta = \arccos(1 - \beta Ca / \mu)$ . As mentioned previously, this model was originally formulated for capillary rise phenomena, which inherently requires  $Ca \geq 0$  and thus only the right-hand part of the curve exists. However, in oscillatory Hele-Shaw flows, the periodic nature permits negative velocity, namely  $Ca < 0$ , leading to  $\cos \theta > 1$ . To avoid this nonphysical phenomenon, a typical approach is expanding around the static state and considering only the varying part (Bongarzone *et al.* 2023), which yields

$$\frac{\partial \eta}{\partial y} = \mp \frac{k b \beta g}{\sigma \Omega} \bar{w}, \quad \text{at } y = \pm \frac{1}{2}. \quad (3.3)$$

The friction coefficient  $\beta$  in (3.3) is a phenomenological parameter that quantifies the dissipation rate resulting from the dynamic wetting process. In fact, (3.3) is the so-called Hocking's model (Hocking 1987) describing a linear variation of the contact angle with the velocity of the contact line. The two extremes  $\beta = 0$  and  $\beta = \infty$  correspond to the free-end and pinned contact line, respectively. For  $\beta = 0$ , the contact line oscillates freely and the friction force does not work, which means the damping of the contact line is zero. For  $\beta = \infty$ , the contact line is always fixed for whatever velocity. This results in the damping approaching infinity and the instability will never emerge. Both limiting cases are not consistent with the dynamics of Faraday waves. In addition, the variation of the contact angle is not always proportional to the velocity in the present problem. From laboratory observations, when forcing acceleration is far below the critical threshold,  $\theta$  varies in a small range around  $\theta_s$ . As the acceleration amplitude increases, this range expands. But the contact line hardly moves before the onset threshold is reached. This phenomenon coincides with the hysteresis feature of the dynamic contact angle, and cannot be captured by Hocking's model (3.3). Once the Faraday linear instability appears, the free surface rises rapidly and, naturally, the contact line moves.

Inspired by Viola *et al.* (2018), we introduce a refined contact angle model to deal with (3.2), which reads

$$\theta = \theta_s + \frac{\Delta}{2} \tanh(\alpha \varepsilon Ca), \quad \text{with } Ca = \frac{\mu}{\sigma} \frac{\Omega}{k} \frac{\partial \bar{\zeta}}{\partial t}. \quad (3.4)$$

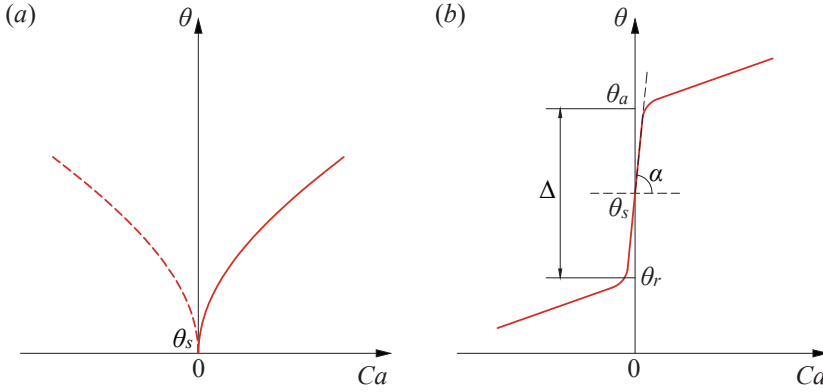


Figure 2. (a) Sketch of the dynamic contact angle model (1.2) developed by Hamraoui *et al.* (2000). (b) Sketch of the contact angle hysteresis model (3.4) developed by Viola *et al.* (2018).

Compared with the definition of  $Ca$  in (1.2), the expression of  $Ca$  in (3.4) is obtained by replacing the vertical velocity of the contact line with that of the gap-averaged free surface and combining with the kinematic condition (2.14). Figure 2b illustrates how (3.4) represents the dynamic contact angle variation within the hysteresis range  $\Delta$  around the static contact angle  $\theta_s$ . The steepness parameter  $\alpha \gg 1$  sets the velocity scale at which the contact angle varies. The effect of pinned contact line is captured by the hyperbolic tangent function. Although the contact line velocity is almost zero prior to Faraday onset, a constitutive relationship between  $\theta$  and  $Ca$  is required to model the contact angle dynamics. The hyperbolic tangent function ensures rapid variation of  $\theta$  at even small velocities and, as long as  $\alpha$  is sufficiently large, the approximation in (3.4) remains consistent with the pinned contact line condition. We note that figure 2b gives a linear variation of  $\theta$  beyond the hysteresis range, indicating a moving contact line. This physical regime corresponds to the fully developed Faraday wave stage and is outside the scope of both (3.4) and linear stability analysis.

Because the fluid field is gap-averaged, one cannot distinguish the contact line motion near the lateral walls from the averaged interface elevation. We utilize the vertical velocity of in-plane Faraday waves to define (3.4). Nevertheless, to bridge these two velocity scales, we introduce a dimensionless coupling coefficient  $\varepsilon$ , which may be treated to be either constant or time-dependent. This process reflects how the gap-averaging method oversimplifies the transverse flow information. In other words, the inclusion of meniscus effects in the gap-averaged normal stress boundary condition (3.1) inherently impedes the accurate modeling of contact angle dynamics.

Consequently, gap-averaged governing equations cannot properly account for contact angle effects, as they crudely approximate the contact line velocity through the gap-averaged vertical velocity of the free surface. The widely used Hamraoui's linear model (1.2) in existing gap-averaging frameworks fundamentally conflicts with the Faraday instability problem. These constraints underscore the critical necessity of gap-resolved analysis in modeling realistic contact angle dynamics.

### 3.2. Governing equations for the gap flow

With both viscous dissipation and gap-averaged damping already taken into account in the amplitude equation (2.21), analysis in this section focuses specifically on the contact angle hysteresis damping. To avoid a redundant calculation of viscous dissipation and the

singularity between contact line motion and the no-slip condition, the potential flow theory is adequate for modeling the gap flow.

Under vertical periodic vibration, equations that govern the dimensional velocity potential  $\phi'$  and meniscus elevation  $\eta'$  are summarized as follows:

$$\frac{\partial^2 \phi'}{\partial x'^2} + \frac{\partial^2 \phi'}{\partial y'^2} + \frac{\partial^2 \phi'}{\partial z'^2} = 0, \quad (3.5a)$$

$$\frac{\partial \phi'}{\partial t'} + (g - a \cos \Omega t') \eta' = \frac{\sigma}{\rho} \left\{ \frac{\partial_{y'y'} \eta'}{\left[1 + (\partial_{y'} \eta'_s)^2\right]^{3/2}} + \frac{\partial_{x'x'} \eta'}{\left[1 + (\partial_{y'} \eta'_s)^2\right]^{1/2}} \right\}, \quad \text{at } z' = 0, \quad (3.5b)$$

$$\frac{\partial \eta'}{\partial t'} + \frac{\partial \eta'_s}{\partial y'} \frac{\partial \phi'}{\partial y'} = \frac{\partial \phi'}{\partial z'}, \quad \text{at } z' = 0, \quad (3.5c)$$

$$\frac{\partial \phi'}{\partial z'} = 0, \quad \text{at } z' = -H, \quad (3.5d)$$

$$\frac{\partial \phi'}{\partial y'} = 0, \quad \text{at } y' = \pm \frac{b}{2}, \quad (3.5e)$$

$$\frac{\partial \eta'}{\partial y'} = \pm \cot \theta, \quad \text{at } y' = \pm \frac{b}{2}, \quad (3.5f)$$

$$\theta = \theta_s + \frac{\Delta}{2} \tanh \left( \alpha \frac{\mu}{\sigma} \frac{\partial \eta'}{\partial t'} \bigg|_{y'=\pm b/2} \right). \quad (3.5g)$$

Equations (3.5b) and (3.5c) are the dynamic and kinematic conditions on the linearized free surface, respectively. Equations (3.5d) and (3.5e) represent the non-penetrable conditions at the solid bottom and lateral walls, respectively. Because a numerical method will be used to solve the governing equations, the solid bottom is set at  $z' = -H$ . This setting remains consistent with (2.9), since the liquid is deep enough that the distinction of the final results between finite and infinite values of  $H$  is negligible. Equations (3.5f) and (3.5g) work for the contact line condition.

Before solving the governing equations (3.5a)-(3.5g), we decompose  $\phi'$ ,  $\eta'$ , and  $\theta$  into their static and perturbed components, namely

$$\phi' = \phi'_s + \phi'_p, \quad \eta' = \eta'_s + \eta'_p, \quad \theta = \theta_s + \theta_p. \quad (3.6a-c)$$

Unlike the perturbed quantities  $\phi'_p$ ,  $\eta'_p$ , and  $\theta_p$  that will be expanded in the asymptotic analysis, the static components  $\phi'_s$ ,  $\eta'_s$ , and  $\theta_s$  correspond to the equilibrium base state. These steady terms remain decoupled from the perturbed parts and consequently do not influence the linear characteristics of (3.5b) and (3.5c). Similar treatment has been successfully implemented in modeling the capillary damping of inviscid surface waves in a circular cylindrical container (Kidambi 2009).

### 3.3. Static meniscus

Without external vibration, the static state satisfies

$$\phi'_s = 0, \quad (3.7a)$$

$$g\eta'_s = \frac{\sigma}{\rho} \frac{\partial_{y'y'}\eta'_s}{\left[1 + (\partial_{y'}\eta'_s)^2\right]^{3/2}}, \quad (3.7b)$$

$$\frac{\partial\eta'_s}{\partial y'} = \pm \cot \theta_s, \quad \text{at } y' = \pm \frac{b}{2}. \quad (3.7c)$$

Equation (3.7b) is nonlinear in  $\eta'_s$  and is solved numerically in MATLAB using an iterative Newton method (Viola *et al.* 2018). Generally speaking, the governing equation (3.7b) is discretized by means of the Chebyshev collocation method on the Gauss-Lobatto-Chebyshev collocation grid  $s \in [-1, 1]$ , which is mapped into the physical space  $y' \in [0, b/2]$  (one can extend to the entire domain region according to symmetry) through a linear mapping  $y' = (s + 1)b/4$ . The differential operators in (3.7b) and (3.7c) are then represented by algebraic matrices. The iterative Newton method includes five steps:

- (i) Define an initial guess solution  $\eta_s^{(0)}$  that satisfies the boundary condition (3.7c).
- (ii) Calculate the residual function  $F(\eta_s^{(i)})$  and the corresponding Jacobian  $J(\eta_s^{(i)}) = dF(\eta_s^{(i)})/d\eta_s^{(i)}$ .
- (iii) Solve for  $\delta\eta'_s$  the linear system  $J(\eta_s^{(i)})\delta\eta'_s = -F(\eta_s^{(i)})$ .
- (iv) Update the solution  $\eta_s^{(i+1)} = \eta_s^{(i)} + \delta\eta'_s$ .
- (v) Compute the  $L_2$ -norm of  $\delta\eta'_s$ . If  $\|\delta\eta'_s\| < 10^{-8}$ , output the solution for  $\eta'_s$ , otherwise, go back to step (ii).

### 3.4. Asymptotic expansion

By introducing an expansion parameter  $\epsilon$ , the physical parameters are expressed as  $\Delta = \epsilon\hat{\Delta}$ ,  $a = \epsilon\hat{a}$ , and  $\alpha\mu/\sigma = \hat{\alpha}/\epsilon$ . These physical quantities are rescaled in order to incorporate, as much as possible, all the features of the contact line law (3.5g), for instance, a small hysteresis range and a rapid variation of contact angle at sufficiently small contact line velocity.

We present an asymptotic analysis of the perturbed components governed by (3.5a)-(3.5g). The variables are expanded as

$$\phi'_p = \phi'_{p1} + \epsilon\phi'_{p2} + O(\epsilon^2), \quad \eta'_p = \eta'_{p1} + \epsilon\eta'_{p2} + O(\epsilon^2), \quad \theta_p = \theta_{p1} + \epsilon\theta_{p2} + O(\epsilon^2). \quad (3.8a-c)$$

The multiple scale approach (Nayfeh 1993) is also employed in this section. Hence, we have a slow time scale  $T' = \epsilon t'$  and  $\partial_{t'} \rightarrow \partial_{t'} + \epsilon\partial_{T'}$ .

#### 3.4.1. Order $\epsilon^0$

At order  $\epsilon^0$ , the free-edge boundary condition is considered at the contact line, which means  $\theta_{p1} = 0$  and, (3.5f) reduces to

$$\frac{\partial\eta'_{p1}}{\partial y'} = 0, \quad \text{at } y' = \pm \frac{b}{2}. \quad (3.9)$$

The dynamic condition (3.5b) at this order reads

$$\frac{\partial\phi'_{p1}}{\partial t'} + g\eta'_{p1} - \frac{\sigma}{\rho} \left\{ \frac{\partial_{y'y'}\eta'_{p1}}{\left[1 + (\partial_{y'}\eta'_s)^2\right]^{3/2}} + \frac{\partial_{x'x'}\eta'_{p1}}{\left[1 + (\partial_{y'}\eta'_s)^2\right]^{1/2}} \right\} = 0, \quad \text{at } z' = 0. \quad (3.10)$$

Remaining equations for  $\phi'_{p1}$  and  $\eta'_{p1}$  that have the same form as (3.5a), and (3.5c)-(3.5e) are not listed again. To solve the equations at this order, the ansatzes are written as

$$\phi'_{p1}(x', y', z', t', T') = B'(T') \sin(kx') \check{\phi}'_{p1}(y', z') e^{i\Omega t'/2} + \text{c.c.}, \quad (3.11a)$$

$$\eta'_{p1}(x', y', t', T') = B'(T') \sin(kx') \check{\eta}'_{p1}(y') e^{i\Omega t'/2} + \text{c.c.}, \quad (3.11b)$$

where  $B'(T')$  is the real amplitude that represents the modulation of the evolution of free surface on a slow time scale. Because the theory focuses on the critical condition for the subharmonic Faraday instability, the ansatzes are constructed to include the subharmonic mode, consistent with the assumption introduced in § 2. Substituting (3.11a) and (3.11b) into the governing equations, we obtain a system of equations about the spatial variables  $\check{\phi}'_{p1}$  and  $\check{\eta}'_{p1}$ , which are solved numerically by means of a spectral method (Viola *et al.* 2016, 2018). We refer to Appendix A for details on the numerical method and associated convergence analysis. During the numerical solving process at this order, the values of  $k$  must be specified in advance. Recalling that a traditional dispersion relation has been introduced at the same order in § 2.2, we adopt the results of  $k$  calculated from this formulation.

### 3.4.2. Order $\epsilon$

At order  $\epsilon$ , the form of (3.5a), (3.5d), and (3.5e) will not change, while (3.5b), (3.5c), and (3.5f) read

$$\frac{\partial \phi'_{p2}}{\partial t'} + g\eta'_{p2} - \frac{\sigma}{\rho} \left\{ \frac{\partial_{y'y'}\eta'_{p2}}{\left[1 + (\partial_{y'}\eta'_s)^2\right]^{3/2}} + \frac{\partial_{x'x'}\eta'_{p2}}{\left[1 + (\partial_{y'}\eta'_s)^2\right]^{1/2}} \right\} = -\frac{\partial \phi'_{p1}}{\partial T'}, \quad \text{at } z' = 0, \quad (3.12a)$$

$$\frac{\partial \eta'_{p2}}{\partial t'} + \frac{\partial \eta'_s}{\partial y'} \frac{\partial \phi'_{p2}}{\partial y'} - \frac{\partial \phi'_{p2}}{\partial z'} = -\frac{\partial \eta'_{p1}}{\partial T'}, \quad \text{at } z' = 0, \quad (3.12b)$$

$$\frac{\partial \eta'_{p2}}{\partial y'} = \mp \frac{\theta_{p2}}{\sin^2 \theta_s}, \quad \text{at } y' = \pm \frac{b}{2}, \quad (3.12c)$$

with

$$\theta_{p2} = \frac{\hat{\Delta}}{2} \tanh \left( \frac{\hat{\alpha}}{\epsilon} \frac{\partial \eta'_{p1}}{\partial t'} \bigg|_{y'=b/2} \right). \quad (3.13)$$

At this order, an amplitude equation that involves the contact angle hysteresis damping will be obtained. Since we are only concerned with the expression for the capillary damping in this section, which will be incorporated into (2.21) for the stability analysis, the external forcing term  $\hat{a} \cos \Omega t' \eta'_{p1}$  is not explicitly written in (3.12a). The ansatzes of  $\phi'_{p2}$  and  $\eta'_{p2}$  are written as

$$\phi'_{p2}(x', y', z', t', T') = \sin(kx') \check{\phi}'_{p2}(y', z', T') e^{i\Omega t'/2} + \text{c.c.}, \quad (3.14a)$$

$$\eta'_{p2}(x', y', t', T') = \sin(kx') \check{\eta}'_{p2}(y', T') e^{i\Omega t'/2} + \text{c.c.} \quad (3.14b)$$

We then introduce an adjoint global mode  $\mathbf{q}_1^\dagger = (\phi_{p1}^\dagger, \eta_{p1}^\dagger)^\text{T}$  to obtain the solvability condition based on the Fredholm alternative. By means of the Fourier expansion, the tangent function in (3.13) is properly treated to preserve hysteresis effects. The detailed

derivation of the solvability condition and treatment of (3.13) are given in Appendix B. With these efforts, an amplitude equation is obtained, which reads

$$\frac{dB'}{dT'} + \frac{2i \sin \theta_s \hat{\Delta} \sigma \kappa}{\pi \rho |\check{\eta}'_{p1}|_{y'=b/2}} \frac{B'}{|B'|} = 0, \quad \text{with } \kappa = \frac{\eta_{p1}^{\dagger*} \check{\eta}'_{p1} \big|_{y'=b/2}}{\int_{-b/2}^{b/2} \left( \eta_{p1}^{\dagger*} \check{\phi}'_{p1} + \phi_{p1}^{\dagger*} \check{\eta}'_{p1} \right) \big|_{z'=0} dy'}. \quad (3.15)$$

In accordance with the approach established in § 2, we nondimensionalize (3.15) using  $k^{-1}$  and  $\Omega^{-1}$  as the characteristic length and time, respectively. The resulting dimensionless amplitude equation reads

$$\frac{dB}{dT} + \chi B = 0, \quad \text{with } \chi = \frac{2i \sin \theta_s \hat{\Delta} \sigma \kappa}{\pi \rho \Omega |\check{\eta}'_{p1}|_{y'=b/2} |B'|}. \quad (3.16)$$

The amplitude equation (3.15), which exclusively accounts for the dissipation originating from contact angle dynamics, indicates that capillary hysteresis damping depends solely on the contact line velocity through its sign. This behavior, as pointed out by Miles (1967) and Noblin *et al.* (2004), can be interpreted as a Coulomb-like friction force. To isolate the damping contributions, following the approach used for (2.21), we decompose the complex amplitude  $B$  into modulus and phase, namely  $B = |B| e^{i\Phi}$ , and write the modulus as  $|B| = B_0 e^{-\gamma_2 t}$ . Thus, the damping rate  $\gamma_2$  is calculated by

$$\gamma_2 = -\frac{d \log (|B| / B_0)}{dt} = -\frac{\epsilon}{|B|} \frac{d|B|}{dT} = \epsilon \chi = \frac{2i \sin \theta_s \Delta \sigma \kappa}{\pi \rho \Omega |\check{\eta}'_{p1}|_{y'=b/2} |B'|}. \quad (3.17)$$

Recalling that we have set  $|\check{\eta}'_{p1}|_{y'=0} = 1$ , and combining with the definition of  $B'(T')$  in (3.11a) and (3.11b),  $|B'|$  refers to the magnitude of the real oscillation amplitude of the bottom of the meniscus immediately prior to the onset. Accordingly, (3.17) reveals that the contact angle hysteresis damping depends on the amplitude of the oscillatory meniscus. This fact agrees with the theoretical finding of Viola *et al.* (2017) when studying capillary hysteresis in sloshing dynamics and is consistent with the experimental observation by Keulegan (1959) and Cocciaro *et al.* (1993). The difference is that these studies focused on the wave attenuation caused by the energy dissipation at solid walls. Specifically, the wave amplitude decays from a finite initial value toward zero, accompanied by a damping rate that varies temporally throughout the evolution. But for the Faraday linear stability problem, we are concerned with the critical condition for the onset of free surface, corresponding to the stability of the trivial solution ( $|A| = 0$ ) in the amplitude equation for Faraday waves. We note that a nontrivial value of  $|B'|$  is required to calculate  $\gamma_2$ . As observed experimentally in § 4.1, the meniscus has already oscillated periodically prior to Faraday onset, implying  $|B'| \neq 0$  and  $|A| = 0$ . Because  $|B'|$  cannot be predicted by the present theory, we employ experimentally measured values to calculate this gap-resolved capillary damping in the stability analysis of Faraday waves.

#### 4. Experiments

Currently, we have obtained explicit expressions of the dissipation induced by narrow transverse confinement, contact angle hysteresis effects, and fluid viscosity. Comparison with experiments is required to verify the theoretical framework. On the one hand, the evolution of the meniscus is observed, from which contact angle parameters such as the static contact angle  $\theta_s$  and the hysteresis range  $\Delta$  for three different liquids are obtained. Comparison between numerical results of meniscus dynamics and experimental

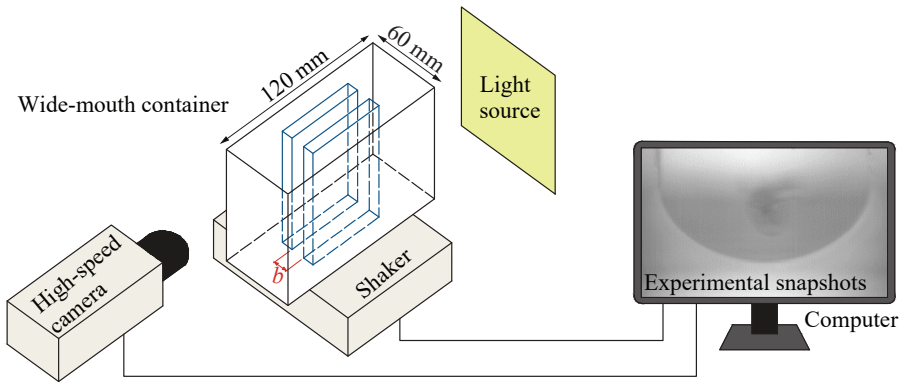


Figure 3. Schematic illustration of the experimental set-up for meniscus experiments, with the camera focused on the meniscus from a side view of the container.

| Liquid               | $\mu$ (mPa s) | $\rho$ (g cm <sup>-3</sup> ) | $\sigma$ (mN cm <sup>-1</sup> ) |
|----------------------|---------------|------------------------------|---------------------------------|
| 99.7% pure ethanol   | 1.0995        | 0.7858                       | 0.2207                          |
| 80% ethanol solution | 2.0271        | 0.8529                       | 0.2578                          |
| 70% ethanol solution | 2.2249        | 0.8788                       | 0.2735                          |

Table 1. Fluid parameters of the working liquids. Data are taken from Khattab *et al.* (2012).

observations is also presented. On the other hand, Faraday instability experiments are performed in Hele-Shaw cells made of the same material as the container used in meniscus experiments, with direct measurements of the onset parameters.

The sketches of the experimental set-up are depicted in figure 3 and 7. A container made of polyvinyl chloride (PVC) filled with liquids is fixed on an electrodynamic vibration generator (ESS-050), which can provide a peak force of 500 N and impose a vertical sinusoidal oscillation of acceleration  $a \cos \Omega t'$ , with  $\Omega = 2\pi f$ , and  $f$  denoting the driving frequency. A closed-loop system is utilized to control the vibration of the shaker through a computer, which guarantees a waveform deviation factor within 0.3% and a driving frequency resolution of 0.01%. The free surface is observed and recorded by a high-speed camera at a speed of 500 frames per second. To ensure the illumination intensity and quality of images, a high-frequency lamp is used. The temperature of the room is maintained at around  $25 \pm 1$  °C. Three ethanol-water mixtures are used as working liquids: pure ethanol (> 99.7 wt%), 80 vol% and 70 vol% ( $\pm 1$  vol%) ethanol-water solutions. Their physical properties are listed in table 1.

#### 4.1. Meniscus observation

In meniscus experiments, a wide-mouth container is employed (see figure 3 for the sketch), with a length of 120 mm, a width of 60 mm, and a height of 60 mm. There are two panels made of PVC in the center of this container that form a 4.8 mm gap. Therefore, the meniscus formed in this gap is consistent with that in Hele-Shaw cells. The camera is placed parallel to these panels and focuses on the meniscus. The Hele-Shaw cell is not employed as a working container in this experimental series because of the existence of two ends in the longitudinal direction of the cell. Under the interaction between the liquid and the walls, the free surface is three-dimensional near the ends. If we directly focus on the gap in Hele-Shaw cells, the liquid adhering to the end walls will disrupt the



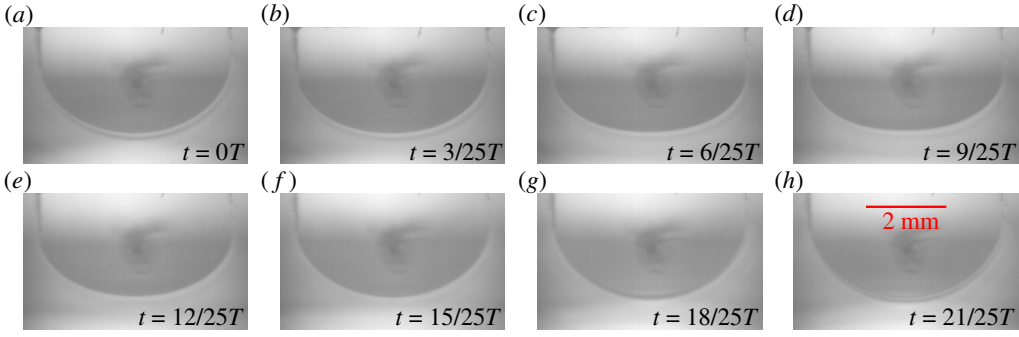


Figure 4. Experimental snapshots of the meniscus for 80% ethanol solution with  $f = 30$  Hz and  $a = 3.9$  m/s<sup>2</sup>. The meniscus oscillates synchronously with the external vibration, implying a period  $T = 1/30$  s. The contact line is nearly fixed, while the contact angle reaches the boundary of the hysteresis range. If the acceleration amplitude is further increased to  $a = 4.0$  m/s<sup>2</sup>, the contact line will move rapidly and Faraday waves emerge.

observation of a two-dimensional meniscus shape. Using such a wide-mouth container, and optimizing focal length to isolate a specific cross-section, a two-dimensional free surface profile between the panels is captured and recorded by the high-speed camera.

The container is filled with the corresponding liquids to a depth of 20 mm and fixed on the vibration generator. Without external vibration, the static contact angle is extracted. When the amplitude of the forcing acceleration is lower than the critical threshold, the observed meniscus oscillates synchronously with the external vibration. Once  $a_c$  is reached, Faraday waves emerge, and the meniscus oscillates at a frequency half that of the external vibration. In this circumstance, the contact line moves rapidly and the contact angle exceeds the hysteresis range. Therefore, experimental data obtained at acceleration levels just a step (0.1 m/s<sup>2</sup>) below the critical threshold  $a_c$  are used to extract the hysteresis range. The temporal evolution of the meniscus profile under specified vibration parameters just before Faraday onset is presented in figure 4. In this configuration, the contact line remains almost pinned on the lateral walls, while the central region of the meniscus undergoes up-and-down motions. Near the equilibrium position (figure 4a,h), the meniscus profile closely approximates a circular arc, but at maximum elevation (figure 4d), the central region is significantly flattened.

To automatically extract the dynamic contact angle from the high-speed video frame by frame, a customized MATLAB program based on the polynomial fitting approach is developed (Kalantarian *et al.* 2011; Shen *et al.* 2024). For each experimental snapshot, the meniscus profile is extracted by means of the Canny edge detector and then approximated with a sixth-order polynomial curve fitted with 260 pixels. The contact angle is determined by the derivative of the polynomial fit at the lateral wall positions, followed by averaging the values obtained from both sides of the gap. We refer to Appendix C for detailed image processing steps.

Through this technique, we obtain the temporal evolution of the contact angle, which is shown in figure 5. Fourier-fitted curves are superimposed on the experimental data to suppress high-frequency noise and elucidate the underlying trend. The contact angle varies periodically between its maximum and minimum values, namely the advancing and receding contact angles. Far from the limiting values, the contact angle varies rapidly. As it approaches the hysteresis boundary, the rate of variation decreases significantly. As a result, these signals exhibit an intermediate shape between sinusoidal and square wave patterns. This trend is consistent with the expected dynamic wetting behavior observed by Cocciano *et al.* (1993) and Shen *et al.* (2024).

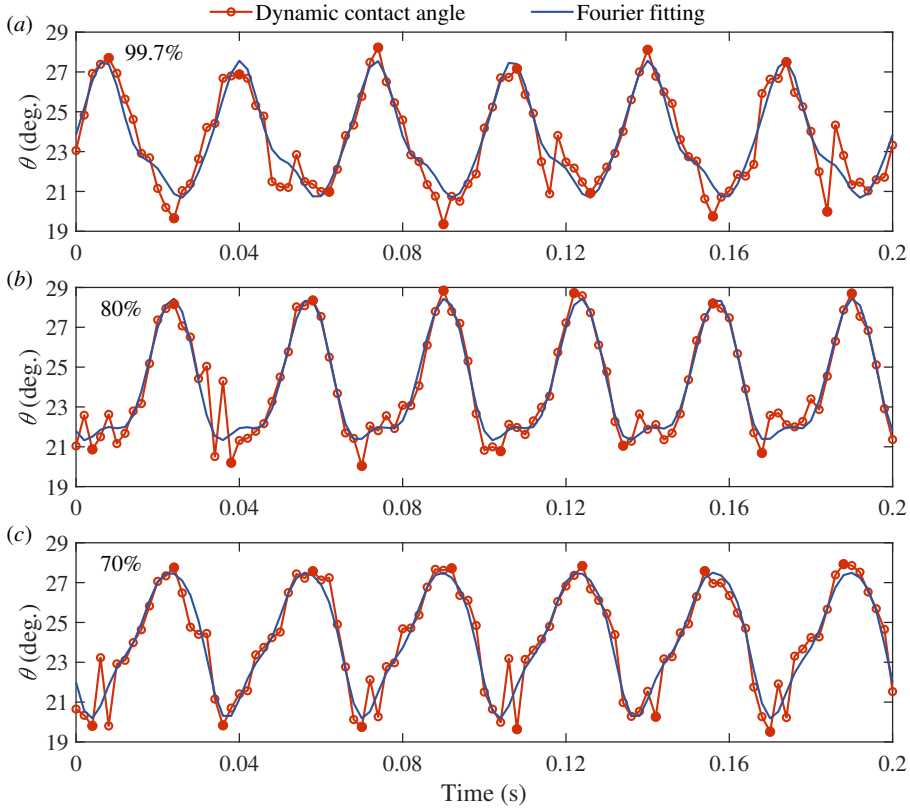


Figure 5. Temporal variation of the contact angle under 30 Hz external vibration for various liquids in the PVC container. (a) Pure ethanol, with  $a = 3.4 \text{ m/s}^2$ . (b) 80 vol% ethanol solution, with  $a = 3.9 \text{ m/s}^2$ . (c) 70 vol% ethanol solution, with  $a = 4.1 \text{ m/s}^2$ . Red lines with circles represent for the experimental data in six cycles. In order to make the trend of  $\theta$  more obvious, we perform Fourier fitting to the third-order on these data and eliminate local deviation, which are plotted with blue lines. Red filled dots identify the maximum and minimum values of  $\theta$  in one cycle and correspond to the advancing and receding contact angles.

| Liquid               | $\theta_s$ (deg.) | $\theta_a$ (deg.) | $\theta_r$ (deg.) | $\Delta$ (deg.) |
|----------------------|-------------------|-------------------|-------------------|-----------------|
| 99.7% pure ethanol   | $25.04 \pm 0.77$  | $27.60 \pm 0.72$  | $20.11 \pm 0.88$  | $7.49 \pm 1.60$ |
| 80% ethanol solution | $25.91 \pm 0.81$  | $28.49 \pm 0.35$  | $20.60 \pm 0.57$  | $7.89 \pm 0.91$ |
| 70% ethanol solution | $26.15 \pm 1.15$  | $27.73 \pm 0.20$  | $19.80 \pm 0.46$  | $7.93 \pm 0.61$ |

Table 2. Contact angle parameters of pure ethanol and its solutions in the PVC container.

For each kind of liquid, the six maximum values as shown in figure 5 are averaged as the advancing contact angle  $\theta_a$ , while the six minimum values are averaged as the receding contact angle  $\theta_r$ . The hysteresis range is then calculated by  $\Delta = \theta_a - \theta_r$ . The static contact angle  $\theta_s$  is extracted from the snapshots that record the static free surface and has been averaged with repeated experiments. Measurements of these parameters are listed in table 2. Yang *et al.* (2024) once studied the wettability property of ethanol-water solutions on hydrophobic highly oriented pyrolytic graphite and found that the contact angle decreases with increasing volume percentage of ethanol, consistent with our measured  $\theta_s$ .

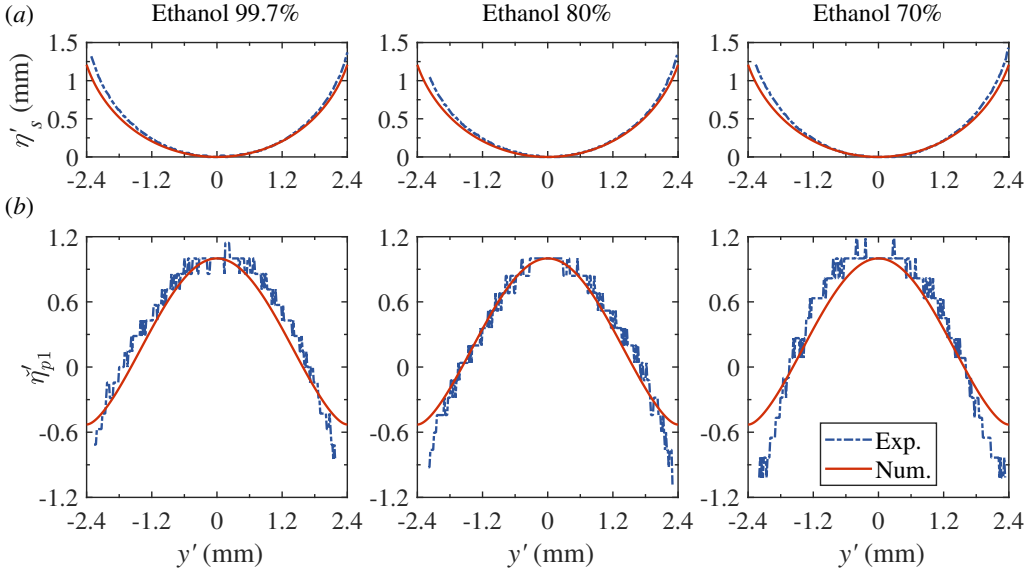


Figure 6. Comparison of meniscus dynamics for three working liquids: experimental observations (chain lines) versus numerical solutions (solid lines). (a) Static meniscus profiles  $\eta'_s$ . (b)  $\epsilon^0$ -order results of  $\eta'_{p1}$ , normalized by imposing that  $\eta'_{p1}(0) = 1$ .

Furthermore, meniscus profiles are extracted from experimental snapshots (e.g., figure 4) and compared with numerical results. The static meniscus is obtained directly from the frames without external vibration. The maximum oscillatory displacement is then calculated by subtracting this static profile from the extreme meniscus position observed during vibration. Recalling that the equations governing the static meniscus (3.7b) and the  $\epsilon^0$ -order problem in § 3.4.1 are solved numerically, using the experimentally measured contact angle parameters in table 2, we obtain the numerical results of  $\eta'_s$  and  $\eta'_{p1}$ . In figure 6a, theory developed for the static meniscus shows good agreement with experiments, particularly for the lower part. The heights of the meniscus are nearly identical, which verifies the measured  $\theta_s$ . In figure 6b, results of  $\eta'_{p1}$  are normalized by setting  $\eta'_{p1}(0) = 1$ . The shape of the oscillatory meniscus is basically captured by the theory, except for the region near the lateral walls. At order  $\epsilon^0$ , the free-edge boundary condition (3.9) is imposed on the free surface, implying a shape always orthogonal to the wall, which is absent in experiments.

#### 4.2. Faraday onset

In Faraday instability experiments, traditional rectangular Hele-Shaw cells are utilized (see figure 7 for the sketch), with a length of 300 mm and a height of 60 mm. Two different gap sizes are adopted, one of 2 mm and the other of 4.8 mm. The camera is placed perpendicular to the lateral wall of the cell, hence only the Faraday wave profile is observed. We concentrate on the critical acceleration amplitude  $a_c$  and the critical wavenumber  $k_c$  of linear instability of the free surface. Following the experimental procedure of Douady & Fauve (1988) and Li *et al.* (2019a), we gradually increase the external acceleration amplitude  $a$  by a step of  $0.1 \text{ m/s}^2$  with a fixed driving frequency  $f$ . At each level of acceleration amplitude, we wait for 1000 periods of the waves, which is regarded as the growth time for the onset. When Faraday waves emerge, the acceleration amplitude is recorded as the threshold  $a_c$ , and the corresponding wavenumber is measured as the

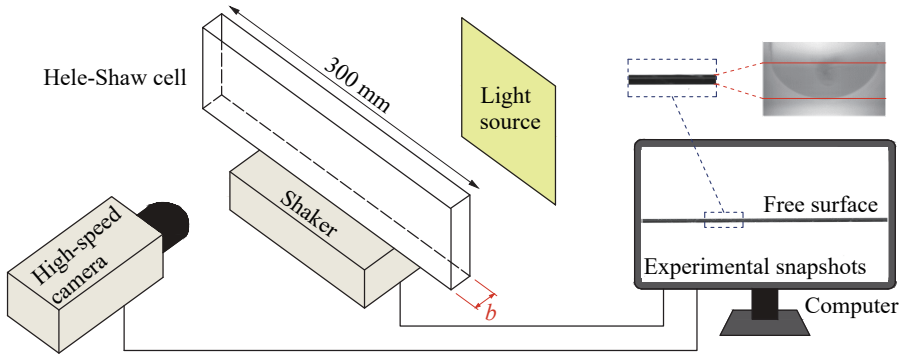


Figure 7. Schematic illustration of the experimental set-up for Faraday instability experiments, with the camera focused on the free surface from a front view of the Hele-Shaw cell.

critical wavenumber  $k_c = 2\pi/L_c$ , with  $L_c$  denoting the critical wavelength of Faraday waves. Each experiment is repeated three times.

The real oscillation amplitude of the bottom of the meniscus  $|B'|$  is measured by the experimental setup used in this section. From experimental snapshots in Faraday instability experiments (e.g., figure 7), the free surface is recorded by a distinct black band with a specific width. The upper edge of this band corresponds to the contact line between the liquid and the lateral walls, while the lower edge corresponds to the bottom of the meniscus, implying that the width of the black band reflects the height of the meniscus. The temporal evolution of the bottom of the meniscus is therefore tracked by monitoring the motion of the lower edge of the black band and extracted over a sufficiently long sequence of snapshots. An experimental example of this evolution is plotted in figure 8. Before onset, the meniscus bottom oscillates periodically with a stable amplitude, exhibiting short-term stability and slowly increasing over longer time scales. Once Faraday waves emerge, the oscillation amplitude increases abruptly. We select the stable interval immediately preceding this rapid increase as the effective measurement range to determine  $|B'|$ , corresponding to a stage in which Faraday waves have not formed yet. The measured values of  $|B'|$  for different working liquids and gap sizes, obtained across all experimental driving frequencies, are summarized in table 3. Besides, figure 8 elucidates the frequency modulation of the subharmonic Faraday instability mode. Well before the moment of onset, the free surface oscillates synchronously with the external vibration. As time progresses, one crest of oscillation diminishes while the other one develops gradually, eventually leading to the formation of Faraday waves. This process results in the observed wave motion with a frequency half the driving frequency, conforming its subharmonic nature. It should be clarified that one of the crests has nearly vanished in the measurement interval, justifying the assumption of a subharmonic mode in ansatzes (3.11a) and (3.11b).

In the present theory, the Hele-Shaw cell is assumed to be infinite in length, which results in the periodic condition in  $x'$ -direction. However, the presence of two ends in the longitudinal direction may influence the results of linear stability analysis. Bongarzone *et al.* (2023) once employed a thin annulus container to eliminate the effect of two ends. But they imposed that the azimuthal wavenumber is always an integer. Hence, these experiments are limited for identifying the change of  $a_c$  and  $k_c$  induced by the ends of the cell. Here, we employ a shorter Hele-Shaw cell, which has a length of 100 mm. In this case, the container is not so long compared with the wavelength, and the influence of the ends is more significant. As shown in figure 9a, for different cell lengths, the critical acceleration  $a_c$  is generally consistent, except for the case of  $f = 14$  Hz. At this driving frequency, the

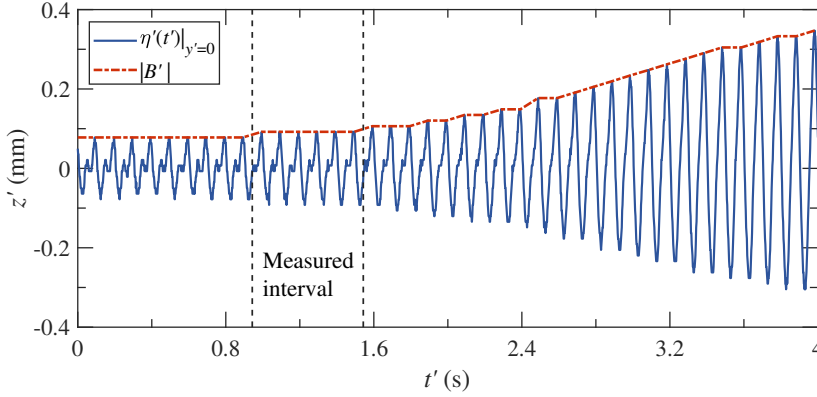


Figure 8. Temporal evolution of the bottom of the meniscus  $\eta'(t')|_{y'=0}$  (solid line) and the real amplitude  $|B'|$  on a slow time scale (chain line). Two vertical dashed lines demarcate the measurement interval for  $|B'|$ . Results show experimental data for 80% ethanol solution in a cell with  $b = 2$  mm, measured at a driving frequency of  $f = 20$  Hz.

| Driving frequency<br>$f$ (Hz) | $b = 2$ mm |        |        | $b = 4.8$ mm |        |        |
|-------------------------------|------------|--------|--------|--------------|--------|--------|
|                               | 99.7%      | 80%    | 70%    | 99.7%        | 80%    | 70%    |
| 10                            | 0.2428     | 0.2254 | 0.2264 | 0.3894       | 0.3273 | 0.3261 |
| 12                            | 0.1792     | 0.1694 | 0.1557 | 0.2781       | 0.2298 | 0.2174 |
| 14                            | 0.1466     | 0.1275 | 0.1203 | 0.2364       | 0.1950 | 0.1902 |
| 16                            | 0.1303     | 0.1133 | 0.1132 | 0.2086       | 0.1671 | 0.1630 |
| 18                            | 0.1140     | 0.0978 | 0.0920 | 0.1669       | 0.1393 | 0.1359 |
| 20                            | 0.1000     | 0.0921 | 0.0849 | 0.1460       | 0.1253 | 0.1223 |
| 22                            | 0.0947     | 0.0832 | 0.0849 | 0.1252       | 0.1114 | 0.1087 |
| 24                            | 0.0868     | 0.0779 | 0.0773 | 0.1182       | 0.1044 | 0.1019 |
| 26                            | 0.0814     | 0.0708 | 0.0708 | 0.0973       | 0.0905 | 0.0883 |
| 28                            | 0.0733     | 0.0638 | 0.0637 | 0.0834       | 0.0801 | 0.0815 |
| 30                            | 0.0706     | 0.0602 | 0.0637 | 0.0807       | 0.0780 | 0.0815 |

Table 3. Experimental results of the real oscillation amplitude of the meniscus  $|B'|$  measured in mm. The measurement error is approximately  $\pm 0.0071$  mm, primarily resulting from the resolution of the imaging system.

experimental wavelength  $L_c$  is not small relative to the cell length  $L$ , and  $L$  is closest to an integer multiple of  $L_c$  ( $L \approx 2.85L_c$ ). This unique length-scale relationship, absent at other frequencies, may explain the observed discrepancy between different  $L$  at  $f = 14$  Hz. When the cell length is increased to 300 mm, the impact of the ends can be basically ignored. A more detailed examination of this phenomenon lies outside the scope of this work. When it comes to the critical wavenumber, from figure 9b, we can conclude that the ends of the cell do not affect the dispersion relation at all. Based on the comparisons of  $a_c$  and  $k_c$  between two different cell lengths, the use of containers with a length of 300 mm guarantees that the Hele-Shaw cell is sufficiently long to make the effect of two ends negligible when modeling the Faraday instability problem.

As we have emphasized before, contact angle hysteresis damping plays an important role in the threshold of Faraday instability and is related to the static contact angle and hysteresis range. These parameters depend on both the liquid (Yang *et al.* 2024) and the solid substrate (Shen *et al.* 2024). If we change the material of the Hele-Shaw cell, the

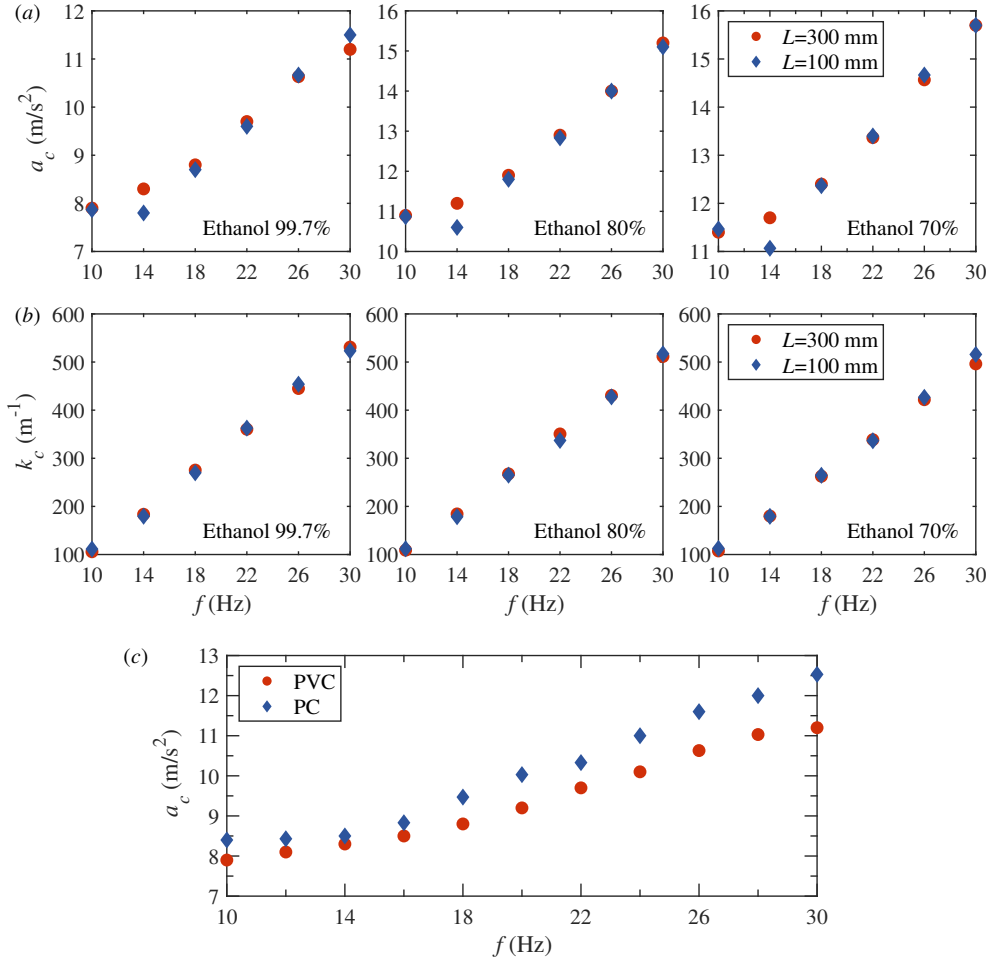


Figure 9. (a) Comparison of the experimental results on  $a_c$  for different cell length  $L$ . Three different ethanol solutions are used, and  $b = 2$  mm. (b) Comparison of the experimental results on  $k_c$  for different  $L$ . The working liquids and gap size are consistent with those in (a). (c) Comparison of the experimental results on  $a_c$  for different materials of the Hele-Shaw cell. Pure ethanol is used as the working liquid, and  $b = 2$  mm.

contact angle parameters will naturally change, leading to the variation of  $a_c$ . This may give intuitive evidence of the impact of dynamic wetting on Faraday waves. Therefore, we conduct experiments in Hele-Shaw cells made of different materials, one of PVC and the other of polycarbonate (PC). As shown in figure 9c, with only the material changing, the values of  $a_c$  are different. This discrepancy cannot be attributed to viscosity or gap-averaged damping, and indicates the significance of contact angle on the Faraday instability problem in Hele-Shaw cells. The comparison also reflects the limitation of the widely used Hamraoui's model (1.2) by Li *et al.* (2019a), Bongarzone *et al.* (2023), and Li & Li (2024), in which the friction coefficient  $\beta$  is only determined by the liquid (Hamraoui *et al.* 2000). This dynamic contact angle model cannot explain the discrepancy in figure 9c. In addition, noting that  $\beta = 0.04$  Pa s for pure ethanol is obtained using glass capillaries as elucidated by Hamraoui *et al.* (2000), it is not rigorous to directly apply the experimental measurements of  $\beta$  in glass containers to the contact angle dynamics in PVC containers. These wetting

parameters must be experimentally measured using containers made of identical materials to those employed in Faraday instability experiments.

## 5. Results and discussion

### 5.1. Stability analysis

In § 2, an amplitude equation for Faraday waves is derived, which contains the damping of the fluid viscosity and the confinement of two lateral walls. Meanwhile, in § 3, another amplitude equation is derived that contains only the damping of contact angle hysteresis effects. All of these damping sources should be taken into account in stability analysis. Because the damping constitutes an intrinsic property of the system that remains independent of amplitude, it is feasible to incorporate the damping term in (3.16) directly into (2.21), which results in the combined amplitude equation:

$$\frac{dA}{dT} + \frac{1}{2} \left[ i (\hat{\delta}_{1,r} + i \hat{\delta}_{1,i}) + i \omega_1^2 + 2\hat{\delta} + 2\chi \right] A + \frac{i\hat{a}}{4g(1+l_c^2 k^2)} A^* = 0. \quad (5.1)$$

We employ Lyapunov's first method to examine the stability of the zero solution of the autonomous dynamic system (5.1). This trivial solution represents the rest state of the free surface. When the forcing acceleration exceeds a critical threshold, the rest state cannot remain stable, giving rise to Faraday waves. Around the zero solution, we introduce the perturbation  $\Lambda_i$ , with  $i = 1, 2$  corresponding to (5.1) and its conjugate equation. The perturbation satisfies

$$\frac{d\Lambda_1}{dT} = -\frac{1}{2} \left( 2\hat{\delta} + 2\chi - \hat{\delta}_{1,i} + i \hat{\delta}_{1,r} + i \omega_1^2 \right) \Lambda_1 - \frac{i\hat{a}}{4g(1+l_c^2 k^2)} \Lambda_2, \quad (5.2a)$$

$$\frac{d\Lambda_2}{dT} = -\frac{1}{2} \left( 2\hat{\delta} + 2\chi - \hat{\delta}_{1,i} - i \hat{\delta}_{1,r} - i \omega_1^2 \right) \Lambda_2 + \frac{i\hat{a}}{4g(1+l_c^2 k^2)} \Lambda_1. \quad (5.2b)$$

Assuming  $\Lambda_i = \Lambda_{i,0} e^{\lambda T}$ , an eigenvalue equation is obtained that

$$\lambda^2 + (2\hat{\delta} + 2\chi - \hat{\delta}_{1,i}) \lambda + \frac{1}{4} \left[ (2\hat{\delta} + 2\chi - \hat{\delta}_{1,i})^2 + (\hat{\delta}_{1,r} + \omega_1^2)^2 \right] - \frac{\hat{a}^2}{16g^2(1+l_c^2 k^2)^2} = 0. \quad (5.3)$$

The eigenvalue is solved as

$$\lambda_{\pm} = \frac{1}{2} \left[ -2\hat{\delta} - 2\chi + \hat{\delta}_{1,i} \pm \sqrt{\frac{\hat{a}^2}{4g^2(1+l_c^2 k^2)^2} - (\hat{\delta}_{1,r} + \omega_1^2)^2} \right]. \quad (5.4)$$

The term  $\hat{\delta}_{1,i}$  is relatively small compared with other terms in (5.4). Hence, the solution  $\lambda_-$  is certainly negative. In order to make the rest state asymptotically stable,  $\lambda_+$  must be negative, which leads to a condition for  $\hat{a}$ :

$$|\hat{a}| < 2g(1+l_c^2 k^2) \sqrt{(2\hat{\delta} + 2\chi - \hat{\delta}_{1,i})^2 + (\hat{\delta}_{1,r} + \omega_1^2)^2}. \quad (5.5)$$

For the periodic vertical vibration, different signs of  $\hat{a}$  represent different directions of the acceleration. By multiplying the parameter  $\epsilon$  to (5.5), and combining with the definition (2.15a-c) and (3.16), for a specific value of  $k$ , an analytical expression for the



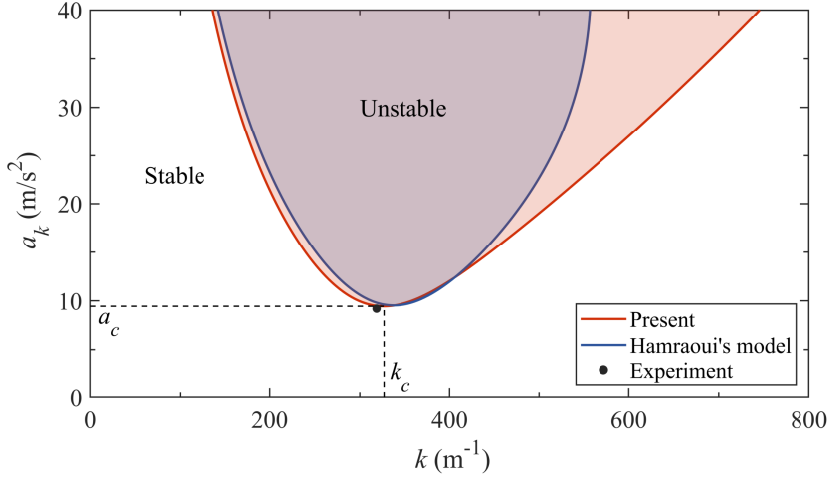


Figure 10. First subharmonic Faraday tongue for pure ethanol in a Hele-Shaw cell of  $b = 2$  mm, with  $f = 20$  Hz. The red unstable region is obtained via (5.6) while blue region is computed by the theory developed by Bongarzone *et al.* (2023) with the employment of Hamraoui's model. Experimental data for this configuration is identified by the black dot. The lowest points on the boundary curves determine the critical parameters  $a_c$  and  $k_c$  for Faraday instability.

homologous acceleration amplitude  $a_k$  is obtained that

$$a_k = 2g \left( 1 + l_c^2 k^2 \right) \sqrt{\left( 2\delta_{St}^2 k^2 b^2 + \frac{4i \sin \theta_s \Delta \sigma \kappa}{\pi \rho \Omega |\tilde{\eta}'_{p1}|_{y'=b/2} |B'|} - \delta_{1,i} \right)^2 + (\delta_{1,r} + \omega^2 - 1)^2}. \quad (5.6)$$

Equation (5.6) reveals that  $a_k$  depends on the fluid properties, contact angle characteristics, and external parametric excitation. For a given set of these parameters,  $a_k$  varies solely with  $k$ . The value of  $a_k$  corresponding to the critical wavenumber  $k_c$  is the critical acceleration amplitude  $a_c$ . Using the method given by Li & Li (2024), we traverse the values of  $k$  in a range of  $0 \sim 1000 \text{ m}^{-1}$ , after which  $a_k$  is computed via (5.6), the minimum of  $a_k$  is then identified as  $a_c$ , and its corresponding wavenumber is regarded as  $k_c$ . Following this procedure, the first subharmonic Faraday instability tongue is obtained as shown in figure 10, which is similar to the one given by Kumar & Tuckerman (1994). For comparison, we include theoretical results obtained using Hamraoui's dynamic contact angle model, which corresponds to the theory developed by Bongarzone *et al.* (2023). In the present experimental configuration, the threshold  $a_c$  obtained by both theories is in good agreement with the experimental one. However, the critical wavenumber  $k_c$  obtained using Hamraoui's model shifts to a higher value compared to the experimental one, while the present model agrees better with the experiment. This unconventional detuning is partially compensated by the current theory. A detailed discussion on the dispersion relation of Faraday waves will be given in the following section.

Now, let us examine the theoretical results of  $a_c$  with experiments in a wide range of driving frequency, which are summarized in figure 11. Li *et al.* (2019a) once performed Faraday instability experiments in Hele-Shaw cells in a frequency range from 14 to 22 Hz. We have extended this range to  $10 \sim 30$  Hz to highlight the trend of  $a_c$ . Theoretically, Bongarzone *et al.* (2023) employed Stokes boundary layer theory when studying the linear stability problem in Hele-Shaw cells, coupled with Hamraoui's model (1.2) to evaluate the damping of the dynamic contact angle. Their theory has currently provided the most



accurate estimation of  $a_c$ . As shown in figure 11, with the utilization of Hamraoui's model, the theory agrees well with experiments, particularly for the case of  $b = 4.8$  mm. However, a remarkable discrepancy in the trend persists, which is more evident for a smaller gap size ( $b = 2$  mm). Hamraoui's model predicts a steeper variation of  $a_c$  with  $f$ , resulting in significantly overestimated theoretical values at high driving frequencies. Bongarzone *et al.* (2023) have validated that the increasing trend of  $a_c$  with  $f$  is mainly controlled by the friction coefficient  $\beta$ , a conclusion also verified by Li & Li (2024). Equation (3.3) implicitly reveals that  $\beta$  serves as a linear coefficient for contact angle damping, implying that the theoretical  $a_c$  is sensitive to  $\beta$ . As validated in figure 9c, the value of  $\beta$  for pure ethanol in PVC containers must be different from the one measured by Hamraoui *et al.* (2000). Figure 12 demonstrates substantial changes in the calculated  $a_c$  for modest  $\beta$  variations ( $0.03 \leq \beta \leq 0.05$ ), which obviously deviate from the experimental results. Consequently, Hamraoui's model lacks physical justification for the Faraday instability problem in Hele-Shaw cells, with its successful application critically depending on values of  $\beta$ .

In contrast, our model adequately takes into account unsteady Stokes flow dynamics, pinned contact line constraints, and full viscous dissipation effects. The contact angle hysteresis damping is obtained by resolving the gap flow independently. According to (5.6), the trend of  $a_c$  versus  $f$  is determined by the static contact angle  $\theta_s$ , the hysteresis range  $\Delta$ , the shape of the meniscus reflected in  $\kappa$  and  $|\tilde{\eta}'_{p1}|_{y'=b/2}$ , and the oscillation amplitude of the meniscus  $|B'|$ . Since we have experimentally measured these parameters and solved for  $\kappa$  and  $|\tilde{\eta}'_{p1}|_{y'=b/2}$  numerically, the present theory better meets the Faraday instability problem. For  $b = 2$  mm (figure 11a), the trend of  $a_c$  shows an improved agreement with the experiments, indicating that compared to Hamraoui's model, the contact angle hysteresis formulation more accurately captures meniscus dynamics. In this configuration, the capillary effects are more prominent. For  $b = 4.8$  mm (figure 11b), the proposed theory exhibits a trend similar to that of Hamraoui's model, with both characterizing the Faraday instability well. Finally, we compare the theoretical results of  $a_c$  with experimental measurements in varying ethanol concentrations and gap sizes. The good agreement shown in figure 13 verifies the applicability of the present model.

## 5.2. Dispersion relation

The dispersion relation serves as a fundamental characteristic of Faraday waves, providing crucial insights into their wavelength selection when the instability develops. Although many studies (e.g., Rajchenbach *et al.* (2011), Rajchenbach & Clamond (2015), Li *et al.* (2018a), and Li *et al.* (2019a)) have tried to modify the classical dispersion relation  $(\Omega/2)^2 = gk_c + \sigma k_c^3/\rho$  for gravity-capillary waves by taking forcing and damping into account, this original formulation gives the most accurate description, as validated by Li & Li (2024). We have also confirmed that the experimental measurements of  $k_c$  rigorously obey the classical dispersion relation throughout the driving frequency range. However, the model proposed by Bongarzone *et al.* (2023) fails to capture this fundamental relationship, as evidenced by the significant discrepancy between their theory and the experiment in figure 14 for the case of  $b = 2$  mm. They also reported a discrepancy between response frequency and driving frequency and found that the Faraday instability tongue shifts toward higher critical wavenumbers (see Figure 4 in Bongarzone *et al.* (2023)). Through asymptotic analysis, they demonstrated that the observed detuning stems from the imaginary component of the gap-averaged damping  $\delta_{1,i}$ , indicating that it is a physically justified and expected phenomenon due to the introduction of oscillatory Stokes flow approximation. This suggests that additional physical mechanisms are required to address

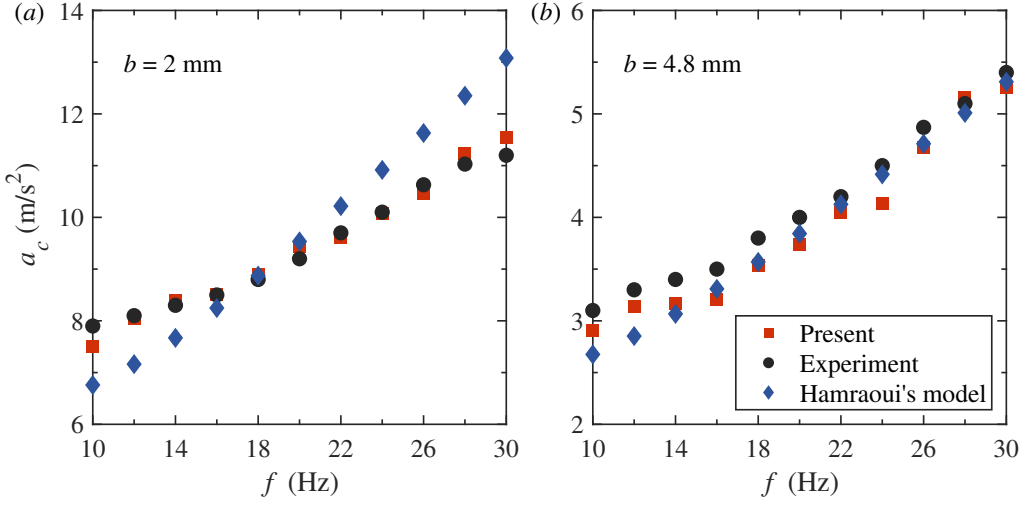


Figure 11. Critical acceleration amplitude  $a_c$  for the onset of Faraday waves versus experimental driving frequency  $f$ . Comparison between theoretical results (squares and diamonds represent results calculated by the present theory and Hamraoui's model used by Bongarzone *et al.* (2023), respectively) and experimental measurements (circles). The working liquid is pure ethanol, while gap size  $b$  is reported in the figure.

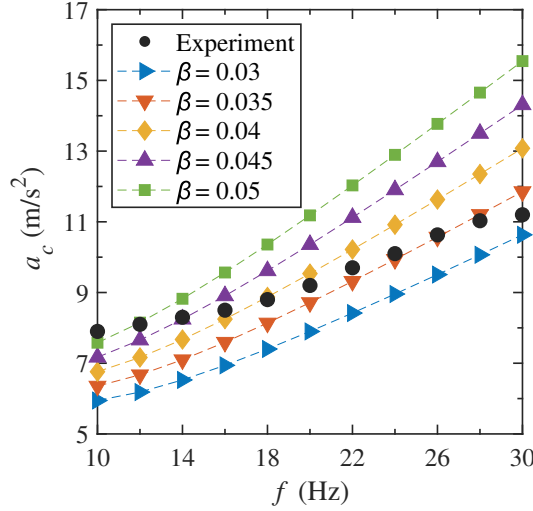


Figure 12. Critical acceleration amplitude  $a_c$  obtained using Hamraoui's model and experimental measurements. Different values of  $\beta$  reported in the figure are used to calculate  $a_c$ . The working liquid is pure ethanol, while  $b = 2$  mm.

the detuning. Although this anomalous phenomenon remains unsolved within existing frameworks, the proposed model provides partial compensation for the detuning. Figure 14 shows slightly better agreement between our theoretical calculations and experimental measurements for arbitrary configurations of liquid and gap size  $b$ . In contrast, Hamraoui's model results in more pronounced detuning at  $b = 2$  mm, particularly for ethanol solutions. The improvement is primarily attributed to the consideration of contact angle hysteresis effects. A brief validation of this conjecture is carried out by setting  $\theta_s = 0^\circ$  or  $\Delta = 0^\circ$  in (5.6), which implies that the contact angle dynamics does not work in stability analysis.

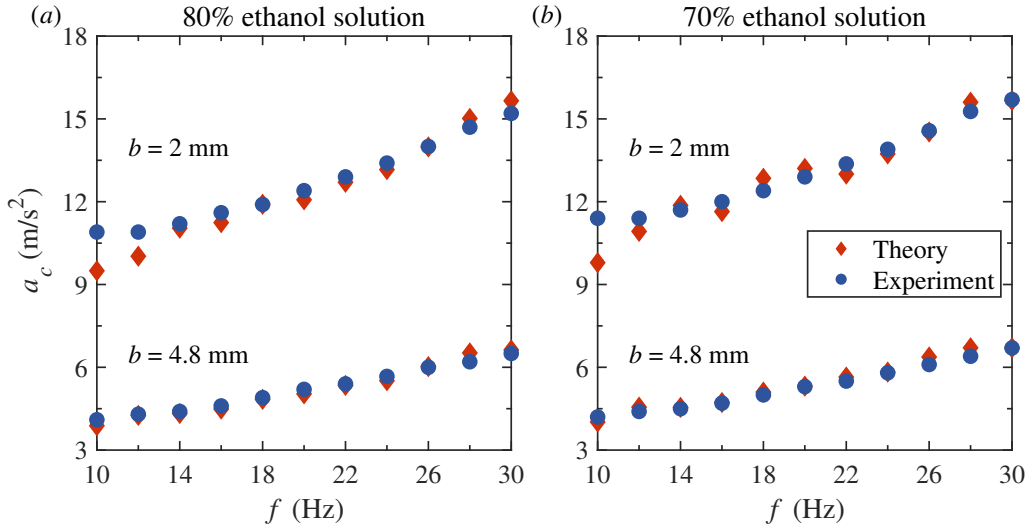


Figure 13. Critical acceleration amplitude  $a_c$  for the onset of Faraday waves versus experimental driving frequency  $f$ . Comparison between the present theoretical results (diamonds) and experimental measurements (circles). The working liquid is 80% ethanol solution for (a) and 70% ethanol solution for (b). Hollow points correspond to the case of  $b = 2$  mm, while filled points correspond to the case of  $b = 4.8$  mm.

The resulting dispersion relation converges to that of Bongarzone *et al.* (2023), and one can refer to the curves corresponding to  $\theta_s = 0^\circ$  and  $\Delta = 0^\circ$  in figure 15 for relevant theoretical results. Therefore, the pinned contact line effects partially counteract the detuning caused by unsteady Stokes flow dynamics. This behavior contrasts markedly with wide-mouth container systems, where both effects are negligible, and the free surface dynamics is governed by gravity and surface tension. Although the observed Faraday waves in Hele-Shaw cells strictly adhere to the classical dispersion relation for gravity-capillary waves, their underlying physical mechanism exhibits fundamental differences.

It should be noted that a slight detuning remains evident in figure 14. This discrepancy is probably attributed to the fact that the proposed theory only captures the initial stage of Faraday instability. The theory aims to characterize the critical condition for Faraday linear stability, corresponding to the moment at which the free surface begins to rise rapidly from a still state. According to (3.5g), only the hysteresis component is considered when modeling the contact angle dynamics, revealing a pinned contact line. However, because the wave pattern arises quickly once the Faraday instability emerges, the experimental data of  $k_c$  are necessarily measured after the onset, during which Faraday waves are already fully developed. In this stage, experimental observations show that the liquid fully wets the lateral walls and a liquid film is formed as the free surface fluctuates, a phenomenon also reported by Li *et al.* (2019a). This change in the wettability condition renders the contact angle hysteresis model no longer applicable. To address the detuning observed in figure 14, alternative mathematical models that better align with the experimental measurement conditions may be effective. Additionally, nonlinear effects associated with large amplitude Faraday waves may also contribute to the observed discrepancy.

Given the substantial influence of contact angle hysteresis effects on the wavelength selection of Faraday waves, we present a discussion in wide ranges of  $\theta_s$  and  $\Delta$ . Since the focus is exclusively on the impacts of contact angle parameters, other input parameters remain constant when varying  $\theta_s$  and  $\Delta$ . The results in figure 15 are obtained using the fluid parameters in table 1 and  $|B'|$  in table 3 for pure ethanol, with a gap size  $b = 2$  mm. On the

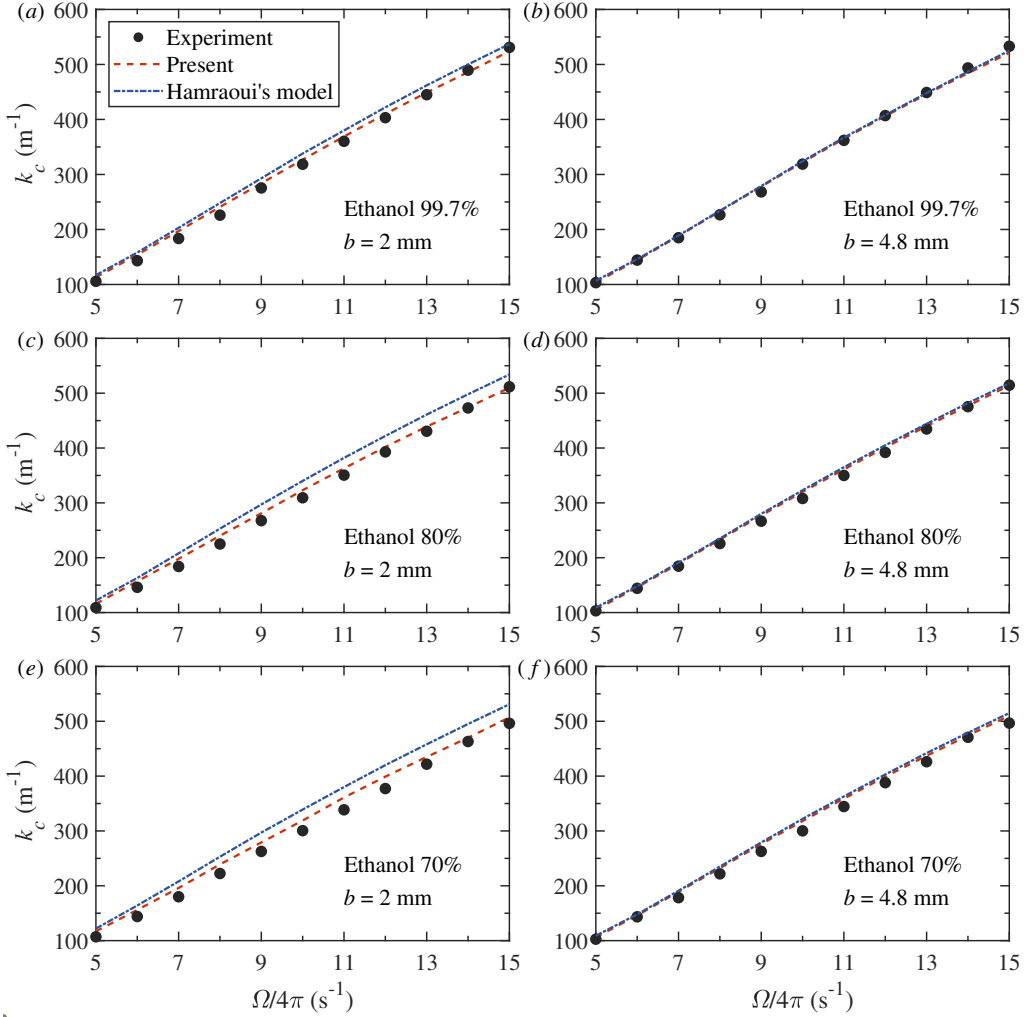


Figure 14. Dispersion relation across different working liquids and gap sizes  $b$ , which are reported in the figure. Comparison between theoretical results (dashed lines: present theory; chain lines: theory developed by Bongarzone *et al.* (2023) using Hamraoui's model, with  $\beta = 0.0538$  for 80% ethanol solution and  $\beta = 0.0597$  for 70% ethanol solution) and experimental measurements (circles). The  $x$ -axis is the response frequency of Faraday waves in subharmonic mode, which is half of the driving frequency  $f = \Omega/2\pi$ .

one hand, we set  $\Delta = 7.49^\circ$  and scan  $\theta_s$  in  $[0^\circ, 90^\circ]$ . Figure 15a shows that the dispersion relation shifts to lower curves as  $\theta_s$  increases. One of the limiting values of  $\theta_s = 90^\circ$  represents a flat profile at rest along the gap direction, that is,  $\eta'_s = 0$ . In other words, the curved static meniscus is completely not taken into account, and the actual surface tension in experiments is significantly underestimated by theory. This case gives the lowest estimation of the dispersion relation, which coincides with the findings presented in Figure 8 of Monsalve *et al.* (2022). The complementary limiting case of  $\theta_s = 0^\circ$  produces a fully curved static meniscus and is related to a complete wetting condition. As mentioned in the previous paragraph, in this strongly hydrophilic regime, contact angle hysteresis effects become negligible, resulting in no modification to the dispersion relation from the contact angle. Considering that  $\cos \theta_s = 1$ , this limiting configuration matches the dynamic contact angle approximation (1.2) proposed by Hamraoui *et al.* (2000). When applying this model

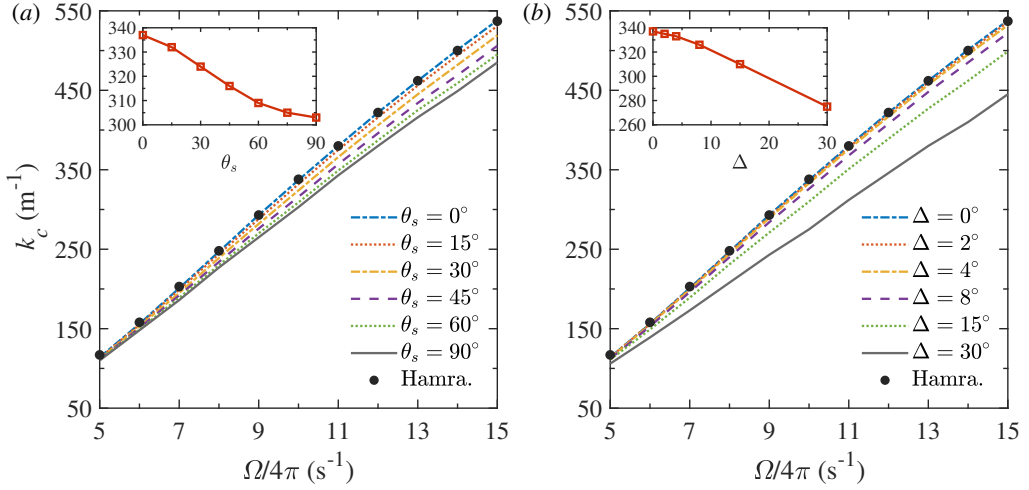


Figure 15. Theoretical dispersion relation for different contact angle parameters. (a) The static contact angle varies from  $0^\circ$  to  $90^\circ$ , with a hysteresis range  $\Delta = 7.49^\circ$ . The inset in (a) shows the critical wavenumber  $k_c$  versus  $\theta_s$  at a response frequency  $\Omega/4\pi = 10$  Hz. (b) The hysteresis range varies from  $0^\circ$  to  $30^\circ$ , with a static contact angle  $\theta_s = 25.04^\circ$ . The inset in (b) shows  $k_c$  versus  $\Delta$  at a response frequency  $\Omega/4\pi = 10$  Hz. Fluid parameters of pure ethanol in table 1 are employed, with  $b = 2$  mm. For comparison, the dispersion relation in figure 14a obtained using Hamraoui's model (Hamra.) is plotted with solid dots.

to the Faraday instability problem, assuming a free dynamics of the contact line fails to capture the physical reality of the contact line pinning and hysteresis effects (Li *et al.* 2019a; Bongarzone *et al.* 2023; Li & Li 2024). Hence, this commonly adopted dynamic contact angle model inadvertently neglects the modifications of meniscus dynamics to dispersion relation. If we focus on a specified response frequency  $\Omega/4\pi = 10$  Hz, as  $\theta_s$  increases, the critical wavenumber reduces to smaller values. The trend is revealed in the inset of figure 15a more clearly, showing a variation that closely follows an inverted sinusoidal shape. This phenomenon is intuitive since the spatial variation of the meniscus strongly depends on the  $y'$ -coordinate as shown in figure 6a, and when  $\theta_s$  approaches  $90^\circ$ , variation of the profile in space is weakened. Hence, the impact of capillary hysteresis on the dispersion relation becomes increasingly pronounced at smaller static contact angles.

On the other hand, we fix  $\theta_s = 25.04^\circ$  and scan  $\Delta$  in  $[0^\circ, 30^\circ]$ , with the results presented in figure 15b. As  $\Delta$  increases, the dispersion relation undergoes qualitatively similar shifts to those observed for varying  $\theta_s$ , but with enhanced magnitudes. These observations demonstrate that the hysteresis range plays a more dominant role in wavelength selection than the static contact angle. The limiting case of  $\Delta = 0^\circ$  implies that the dynamic contact angle maintains a constant value of  $\theta = \theta_s$  prior to onset, according to its expression (3.5g). Once the Faraday instability emerges after overcoming the gap-averaged damping and viscous dissipation, the meniscus oscillates freely without restrictions, completely decoupling the dispersion relation from contact line boundary conditions for whatever values of  $\theta_s$ . For  $\Delta \neq 0^\circ$ , the pinned contact line before onset generates a resistive force in the opposite direction of the meniscus oscillation. This introduces an additional restoring mechanism that, together with gravity and surface tension, changes the phase velocity of the waves, and thereby modifies the dispersion relation. As elucidated by Wilson *et al.* (2022), pinned contact line effects are non-negligible for the frequency shift of Faraday waves, which are absent in Hamraoui's models (1.2). Finally, we concentrate on the response frequency  $\Omega/4\pi = 10$  Hz and find that  $k_c$  decreases approximately linearly

with increasing  $\Delta$ , as shown in the inset of figure 15*b*. This trend arises mathematically due to the linear dependence on  $\Delta$  in the results of the stability analysis (5.6), and noting that  $\Delta$  functions as a linear factor throughout the derivation in § 3.

### 5.3. Damping in Hele-Shaw system

In parametric excitation systems, Faraday waves emerge when the external forcing exceeds a critical threshold, disrupting the equilibrium between energy injection and dissipative losses. In other words, the onset threshold is fundamentally determined by the dissipation, which, in the Hele-Shaw system, includes the gap-averaged damping resulting from the lateral walls, contact angle hysteresis losses at the pinned contact line, two-dimensional viscous dissipation in the fluid bulk, and end-wall boundary effects unique to finite-length rectangular containers. The end-wall boundary effects are excluded from our discussion, since their impact on the instability problem is negligible, as validated by the experimental observations in figure 9*a,b*. The remaining damping contributions are incorporated into the amplitude equations (2.21) and (3.16), with their explicit expressions derived in (2.22) and (3.17). We isolate these damping coefficients according to their distinct physical origins, which read

$$\gamma_{gap} = i(\delta_{1,r} + i\delta_{1,i})/2, \quad \gamma_{hys} = \frac{2i \sin \theta_s \Delta \sigma \kappa}{\pi \rho \Omega |\check{\eta}'_{p1}|_{y'=b/2} |B'|}, \quad \gamma_{vis} = \delta_{St}^2 k^2 b^2. \quad (5.7a-c)$$

Subscripts *gap*, *hys*, and *vis* in (5.7*a-c*) denote, respectively, the gap-averaged damping, contact angle hysteresis dissipation, and bulk viscous dissipation. The damping coefficients  $\gamma_{hys}$  and  $\gamma_{vis}$  are strictly real-valued, as all of their constituent parameters are real except the purely imaginary parameter  $\kappa$ . In contrast, the assumption of oscillatory Stokes flow yields a complex-valued  $\gamma_{gap}$ , the real part of which governs the wave attenuation while the imaginary part induces a detuning and shifts  $k_c$  to higher values (Bongarzone *et al.* 2023). Having discussed this detuning in § 5.2, we now focus exclusively on the real part. Combining with the definition of  $\delta_{1,r}$  and  $\delta_{1,i}$  in (2.22), we obtain the final expression of  $\gamma_{gap}$ , that is,  $\gamma_{gap} = \text{Re} \{ (1 + i) \delta_1 \tanh [(1 + i)/2\delta_1] / 2 \}$ .

Looking at each damping coefficient separately, according to the definition of  $\gamma_{gap}$ , we find that  $\tanh [(1 + i)/2\delta_1] \approx 1$  in current configurations and  $\gamma_{gap}$  is governed by the modified dimensionless thickness of the Stokes boundary layer  $\delta_1 = 2\sqrt{\nu/\Omega}/b$ . Hence, the relationships between  $f$ ,  $b$  and  $\gamma_{gap}$  are scaled as  $\gamma_{gap} \propto f^{-1/2}$ , and  $\gamma_{gap} \propto b^{-1}$ , indicating that  $\gamma_{gap}$  decreases with increasing driving frequency and greater  $b$ .

Then,  $\gamma_{hys}$  is examined. According to (5.7*a-c*), with fixed contact angle parameters,  $\gamma_{hys}$  is determined by  $\kappa$ ,  $|\check{\eta}'_{p1}|_{y'=b/2}$ , and  $|B'|$ . According to the numerical results in Appendix A, we find that both magnitudes of  $\kappa$  and  $|\check{\eta}'_{p1}|_{y'=b/2}$  decrease linearly with increasing  $f$ . The trend of  $\gamma_{hys}$  is then determined by increasing  $\Omega$  and decreasing  $|B'|$ . The variation of these parameters with  $f$  collectively captures the modifications of the meniscus dynamics under different forcing conditions. If Hamraoui's model (1.2) is used, according to Bongarzone *et al.* (2023) and Li & Li (2024),  $\gamma_{hys}$  is replaced by  $\gamma_{ham} = 2k\beta/\rho b\Omega$ . Li *et al.* (2019*a*) observed that  $\gamma_{ham}$  increases monotonically with  $f$ , which ultimately leads to the overestimated trend of  $a_c$  in figure 11. This discrepancy arises naturally due to the limitations of the gap-averaging methodology and Hamraoui's linear contact angle model.

Finally, the bulk viscous dissipation  $\gamma_{vis}$  is discussed. While viscous effects on the Faraday instability have been extensively investigated in three-dimensional systems (e.g., Kumar & Tuckerman (1994); Beyer & Friedrich (1995); Chen & Vinals (1999)), analogous studies in Hele-Shaw configurations are limited to the viscous theory developed by Li & Li (2024). This initial theoretical framework established the complete viscous

governing equations, but the explicit expression for viscous damping remains to be derived. Fortunately, a viscous damping coefficient is obtained in (5.7a-c), which is simplified to  $\gamma_{vis} = 2\nu k^2/\Omega$ . Given the linear relationship  $k \propto f$  satisfied in the current range of  $f$ , we find  $\gamma_{vis} \propto f$ . We also note that  $\gamma_{vis}$  is independent of  $b$  and maintains the same form as in three-dimensional configurations, which is derived by Chen & Vinals (1999). The key distinction lies in the replacement of the two-dimensional wavenumber  $k$  with its three-dimensional counterpart, that is, the wavevector  $\mathbf{k} = (k_x, k_y)$ , where  $k_x$  and  $k_y$  represent the component in the  $x'$  and  $y'$  directions, respectively. The effect of width is manifest for sufficiently large  $b$  that Faraday waves exhibit transverse wave structures across the gap, namely  $k_y \neq 0$ . This phenomenon is not observed in Hele-Shaw experiments, and consequently  $\gamma_{vis}$  is independent of  $b$ .

Before concluding, we give a brief discussion on how key physical parameters (e.g., kinematic viscosity  $\nu$ , surface tension coefficient  $\sigma$ , static contact angle  $\theta_s$ , and contact angle hysteresis range  $\Delta$ ) influence damping in the Hele-Shaw system. According to (5.7a-c), the first parameter  $\nu$  enters the damping through  $\gamma_{gap}$  and  $\gamma_{vis}$ , with scale relationships as  $\gamma_{gap} \propto \nu^{1/2}$  and  $\gamma_{vis} \propto \nu$ . We note that the gap-averaged damping also arises from fluid viscosity, as it is induced by the no-slip condition at lateral walls, where the viscous Stokes boundary layer exists. However, one should distinguish it from the so-called viscous dissipation, which originates from the fluid bulk, as clearly delineated by Li & Li (2024). The other parameters  $\sigma$ ,  $\theta_s$ , and  $\Delta$  act directly on  $\gamma_{hys}$ , as they are all characterized on the free surface. In particular,  $\sigma$  may additionally affect  $\gamma_{vis}$  indirectly through its impact on  $k$  in the dispersion relation. Excluding this potential influence,  $\gamma_{hys}$  exhibits a linear dependence on  $\sigma$ , scaling as  $\gamma_{hys} \propto \sigma$ . In terms of wetting parameters, we have examined that despite the minimal influence of  $\theta_s$  on  $\kappa$  through static state modifications, the contact angle hysteresis dissipation is enhanced for larger  $\theta_s$ , with an approximate trend  $\gamma_{hys} \propto \sin \theta_s$ . For  $\Delta$ , there is an evident relationship in (5.7a-c) that  $\gamma_{hys} \propto \Delta$ , namely the contact angle damping is proportional to the hysteresis range.

## 6. Concluding remarks

Li *et al.* (2019a) confirmed that the effect of the dynamic contact angle dominates over the confinement of the lateral walls in governing Faraday instability problem in Hele-Shaw cells, revealing fundamentally different dynamics from the configuration of wide-mouth containers (Milner 1991). However, existing theoretical frameworks typically rely on the gap-averaged governing equations combined with Hamraoui's linear dynamic contact angle model (Bongarzone *et al.* 2023; Li & Li 2024). Experimental observations of the meniscus suggest that the contact line remains pinned while the meniscus oscillates periodically before Faraday waves emerge, demonstrating that Hamraoui's model results in misrepresented meniscus dynamics and exhibits significant contradictions in oscillatory fluid systems, ultimately yielding inaccurate damping evaluation and an unusual detuning in the dispersion relation.

In this paper, we present a gap-resolved approach that directly deals with the transverse gap flow in Hele-Shaw cells, thereby avoiding oversimplifying contact angle dynamics. A refined contact angle hysteresis model is implemented in boundary conditions at lateral walls, accurately capturing capillary hysteresis in meniscus dynamics. By means of an asymptotic expansion technique, an amplitude equation for the meniscus that explicitly accounts for the contact angle hysteresis damping is derived from governing equations for the gap flow. This damping depends on contact angle parameters (e.g. static contact angle and hysteresis range), numerical solutions and experimental measurements characterizing meniscus dynamics, and external forcing frequency. A novel amplitude equation for Faraday



waves is developed by assuming an oscillatory Stokes flow profile and incorporating contact angle hysteresis damping. Linear stability analysis is conducted by using Lyapunov's first method. Comparison with experiments performed in a wide driving frequency range validates the present theory for addressing the Faraday instability problem in Hele-Shaw cells. This improvement stems from two key factors: the gap-resolved treatment of transverse gap flow and precise measurements of contact angle parameters through meniscus experiments in a container with material properties identical to those used in Faraday instability experiments.

The dispersion relation of Faraday waves in Hele-Shaw cells is strongly influenced by pinned contact line constraints. The pinned contact line exerts a resistive force that alters the dynamics of the free surface, resulting in substantial modifications to the dispersion relation, which so far has not been reported due to limitations of Hamraoui's model. The proposed theoretical model provides partial compensation for the detuning that has persisted since the introduction of Stokes boundary layer theory. Nevertheless, since the formation of a liquid film during experimental measurements of the critical wavenumber indicates a significant change in the wettability condition, and nonlinear features of Faraday waves become more prominent beyond the onset, the mathematical model is recommended to be modified to accurately address the detuning. Moreover, our analysis reveals that contact angle hysteresis damping exhibits a trend governed by competing effects of external forcing and meniscus dynamics, and demonstrates scaling relationships with contact angle parameters, specifically  $\gamma_{hys} \propto \sin \theta_s$  and  $\gamma_{hys} \propto \Delta$ . The gap-averaged damping is quantitatively determined by the dimensionless thickness of the Stokes boundary layer, with a scaling as  $\gamma_{gap} \propto \sqrt{\nu/\Omega}/b$ . Furthermore, we derive for the first time the viscous dissipation of Faraday waves in Hele-Shaw cells, formulated as  $\gamma_{vis} = 2\nu k^2/\Omega$ , which maintains a form similar to the one in wide-mouth containers.

Although the established final relation (5.6) between the critical value of onset and parameters characterizing each physical process is theoretically self-contained and has been verified to be a well-matched model to reveal the generation mechanism and evolution of Faraday instability in Hele-Shaw cells, the validation strongly depends on the laboratory measurements of these parameters, which has been well demonstrated in the present study. Among them, only  $|B'|$  is obtained as the a posteriori value from the experiment, although  $|B'|$  is measured before the onset as the stable stage recognized right before the rapid rise of the free surface. Therefore, in practice, the dependence of  $|B'|$  on other a priori ones becomes a must before utilizing Equation (5.6) to predict the critical acceleration.

**Acknowledgements** We would like to thank Runsheng Chen for help with the laboratory experiments.

**Funding** This work was supported by the National Natural Science Foundation of China (Approval No. 12002206) and the Fundamental Research Funds for the Central Universities.

**Declaration of interests** The authors report no conflict of interest.

## Appendix A. Gap-resolved transverse flow: numerical solutions of $\check{\phi}'_{p1}$ and $\check{\eta}'_{p1}$ at order $\epsilon^0$

In § 3.4.1, the solutions at order  $\epsilon^0$  are obtained numerically. Substituting the ansatzes (3.11a) and (3.11b) into the governing equations at this order, one can obtain a system of equations about the spatial variables  $\check{\phi}'_{p1}$  and  $\check{\eta}'_{p1}$ , whose form in the generalized eigenvalue equation reads

$$\left(\frac{i}{2}\Omega\mathbf{B} - \mathbf{A}\right)\check{\mathbf{q}}'_1 = \mathbf{0}, \quad (\text{A } 1)$$



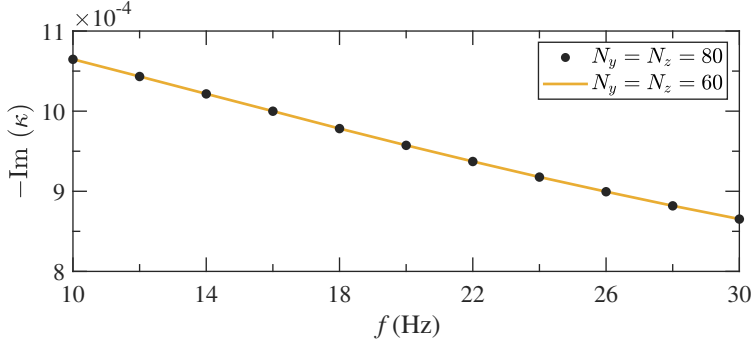


Figure 16. Convergence analysis for the  $\epsilon^0$ -order numerical implementation. Results show the imaginary part of  $\kappa$  calculated by (3.15) against driving frequency  $f$ . The solid line is computed using a  $N_y = N_z = 60$  computational grid, while the dots are obtained with a finer  $N_y = N_z = 80$  computational grid. Physical parameters of pure ethanol are used as inputs, while  $b = 2$  mm.

where  $\check{\mathbf{q}}_1' = (\check{\phi}_{p1}', \check{\eta}_{p1}')^T$  is the eigenvector, and the linear operators are defined by

$$\mathbf{B} = \begin{pmatrix} 0 & 0 \\ \mathbf{I} & 0 \end{pmatrix}, \quad \mathbf{A} = \begin{pmatrix} -k^2 + \frac{\partial^2}{\partial y'^2} + \frac{\partial^2}{\partial z'^2} & 0 \\ 0 & -g\mathbf{I} + \frac{\sigma}{\rho} \left\{ \frac{\partial_{y'y'}}{[1 + (\partial_{y'}\eta_s')^2]^{3/2}} - \frac{k^2}{[1 + (\partial_{y'}\eta_s')^2]^{1/2}} \right\} \end{pmatrix}. \quad (\text{A } 2)$$

Equation (A 1) is restricted by the following boundary conditions:

$$\frac{i}{2}\Omega\check{\eta}_{p1}' - \frac{\partial\check{\phi}_{p1}'}{\partial z'} + \frac{\partial\eta_s'}{\partial y'} \frac{\partial\check{\phi}_{p1}'}{\partial y'} = 0, \quad \text{at } z' = 0, \quad (\text{A } 3a)$$

$$\left. \frac{\partial\check{\phi}_{p1}'}{\partial z'} \right|_{z'=-H} = 0, \quad \left. \frac{\partial\check{\phi}_{p1}'}{\partial y'} \right|_{y'=\pm b/2} = 0, \quad \left. \frac{\partial\check{\eta}_{p1}'}{\partial y'} \right|_{y'=\pm b/2} = 0. \quad (\text{A } 3b-d)$$

The coupled system of the eigenvalue equation and boundary conditions is solved numerically by means of a spectral method (Viola *et al.* 2016, 2018). Linear operators  $\mathbf{B}$  and  $\mathbf{A}$  are discretized using the Chebyshev collocation method. Differential operators in (A 3a) and (A 3b-d) are also discretized via spectral differentiation matrices, and then replace the corresponding rows of the algebraic matrices  $\mathbf{A}$  and  $\mathbf{B}$ . Eventually, (A 1) is solved in MATLAB for the eigenvector  $\check{\mathbf{q}}_1'$ . The eigenvalue in (A 1) corresponds to the response frequency and ultimately leads to a theoretical dispersion relation at this order, although a detailed discussion is not provided here. A grid resolution of  $N_y = N_z = 60$  nodes is employed, which ensures the numerical convergence of the results. For verification of grid convergence, we present in figure 16 the numerical results of  $-\text{Im}(\kappa)$  (with  $\kappa$  defined in (3.15)) obtained using a finer grid  $N_y = N_z = 80$ . Without loss of generality, the solution of  $\check{\mathbf{q}}_1'$  is normalized by setting  $\left| \check{\eta}_{p1}' \right|_{y'=0} = 1$ .

## Appendix B. Gap-resolved transverse flow: solvability condition at order $\epsilon$

In § 3.4.2, an amplitude equation is derived from the solvability condition at order  $\epsilon$ . Substituting the ansatzes (3.14a) and (3.14b) into the governing equations at this order, an equation similar to (A 1) is obtained:

$$\left( \frac{i}{2}\Omega\mathbf{B} - \mathbf{A} \right) \tilde{\mathbf{q}}_2 = \check{\mathbf{D}}_1', \quad (\text{B } 1)$$

with

$$\tilde{\mathbf{q}}_2 = \begin{pmatrix} \check{\phi}_{p2}' \\ \check{\eta}_{p2}' \end{pmatrix}, \quad \check{\mathbf{D}}_1' = \begin{pmatrix} 0 \\ -\frac{\text{d}B'}{\text{d}T'} \check{\phi}_{p1}' \end{pmatrix}. \quad (\text{B } 2a,b)$$

Equation (B 1) is subject to the contact line condition (3.12c) and

$$\frac{i}{2} \Omega \tilde{\eta}'_{p2} - \frac{\partial \tilde{\phi}'_{p2}}{\partial z'} + \frac{\partial \eta'_s}{\partial y'} \frac{\partial \tilde{\phi}'_{p2}}{\partial y'} = -\frac{dB'}{dT'} \tilde{\eta}'_{p1}, \quad \text{at } z' = 0, \quad (\text{B } 3a)$$

$$\left. \frac{\partial \tilde{\phi}'_{p2}}{\partial z'} \right|_{z'=-H} = 0, \quad \left. \frac{\partial \tilde{\phi}'_{p2}}{\partial y'} \right|_{y'=\pm b/2} = 0. \quad (\text{B } 3b,c)$$

To obtain the solvability condition, the adjoint global mode  $\mathbf{q}_1^\dagger = (\phi_{p1}^\dagger, \eta_{p1}^\dagger)^T$  is introduced, which is the solution of the adjoint equation:

$$\left( \frac{i}{2} \Omega \mathbf{B}^\dagger - \mathbf{A}^\dagger \right) \mathbf{q}_1^\dagger = \mathbf{0}, \quad (\text{B } 4)$$

where the linear operators  $\mathbf{A}^\dagger$  and  $\mathbf{B}^\dagger$  are derived by integrating by parts the system of (A 1). Actually, the direct problem at order  $\epsilon^0$  is self-adjoint with respect to the Hermitian scalar product, which means

$$\frac{i}{2} \Omega \mathbf{B}^\dagger - \mathbf{A}^\dagger = -\frac{i}{2} \Omega \mathbf{B} - \mathbf{A}. \quad (\text{B } 5)$$

Therefore, the complex conjugate of the adjoint mode satisfies  $\phi_{p1}^{\dagger*} = \check{\phi}'_{p1}$  and  $\eta_{p1}^{\dagger*} = \check{\eta}'_{p1}$ . The interested readers can refer to Viola *et al.* (2018) for the complete derivation of the adjoint equation and the definition of the adjoint mode.

According to the Fredholm alternative, (B 1) has a nontrivial solution if and only if  $\check{\mathbf{D}}_1'$  is orthogonal to the adjoint mode  $\mathbf{q}_1^\dagger$ , which leads to

$$\left\langle \mathbf{q}_1^\dagger, \left( \frac{i}{2} \Omega \mathbf{B} - \mathbf{A} \right) \tilde{\mathbf{q}}_2 \right\rangle = \left\langle \mathbf{q}_1^\dagger, \check{\mathbf{D}}_1' \right\rangle. \quad (\text{B } 6)$$

The brackets  $\langle \rangle$  defines the Hermitian scalar product:

$$\langle \mathbf{q}_\alpha, \mathbf{q}_\theta \rangle = \int_\Omega \phi_\alpha^* \phi_\theta d\Omega + \int_{-1/2}^{1/2} \eta_\alpha^* \eta_\theta dy. \quad (\text{B } 7)$$

By substituting the expression of  $\check{\mathbf{D}}_1'$  defined in (B 2a,b), the right-hand side of (B 6) reads

$$\left\langle \mathbf{q}_1^\dagger, \check{\mathbf{D}}_1' \right\rangle = -\frac{dB'}{dT'} \int_{-b/2}^{b/2} \eta_{p1}^{\dagger*} \check{\phi}'_{p1} \Big|_{z'=0} dy'. \quad (\text{B } 8)$$

Furthermore, by combining with the boundary conditions (3.12c), (B 3a), and (B 3b,c), the left-hand side of (B 6) is expanded as

$$\begin{aligned} \left\langle \mathbf{q}_1^\dagger, \left( \frac{i}{2} \Omega \mathbf{B} - \mathbf{A} \right) \tilde{\mathbf{q}}_2 \right\rangle &= \left\langle \left( \frac{i}{2} \Omega \mathbf{B}^\dagger - \mathbf{A}^\dagger \right) \mathbf{q}_1^\dagger, \tilde{\mathbf{q}}_2 \right\rangle + \frac{dB'}{dT'} \int_{-b/2}^{b/2} \check{\eta}'_{p1} \phi_{p1}^{\dagger*} \Big|_{z'=0} dy' \\ &\quad - \frac{2\sigma \sin^3 \theta_s}{\rho} \eta_{p1}^{\dagger*} \frac{\partial \tilde{\eta}'_{p2}}{\partial y'} \Big|_{y'=b/2}. \end{aligned} \quad (\text{B } 9)$$

On the right-hand side of (B 9), the first term is zero because of the definition of adjoint equation (B 4), the second term comes from the slow time derivative in the kinematic condition (B 3a), and the last term is associated with the contact line condition (3.12c). The solvability condition (B 6) then reduces to

$$\frac{dB'}{dT'} \int_{-b/2}^{b/2} \left( \eta_{p1}^{\dagger*} \check{\phi}'_{p1} + \phi_{p1}^{\dagger*} \check{\eta}'_{p1} \right) \Big|_{z'=0} dy' - \frac{2\sigma \sin^3 \theta_s}{\rho} \eta_{p1}^{\dagger*} \frac{\partial \tilde{\eta}'_{p2}}{\partial y'} \Big|_{y'=b/2} = 0. \quad (\text{B } 10)$$

To derive the amplitude equation from (B 10), the contact angle at this order (3.13) should be dealt with appropriately. Now that the tangent function is nonlinear, a direct treatment is introducing the Fourier series expansion and separating out the subharmonic modes (Nayfeh 1993; Viola *et al.* 2018):

$$\tanh \left( \frac{\hat{\alpha}}{\epsilon} \frac{\partial \eta'_{p1}}{\partial t'} \Big|_{y'=b/2} \right) = \tanh \left[ \frac{\hat{\alpha}}{\epsilon} \frac{i}{2} \Omega B' \check{\eta}'_{p1} \Big|_{y'=b/2} e^{i(\Omega t'/2 + kx')} + \text{c.c.} \right] = \sum_{n=-\infty}^{\infty} d_n e^{in\Omega t'/2}. \quad (\text{B } 11)$$

If we decompose the complex amplitude  $B'$  and  $\check{\eta}'_{p1}$  in modulus and phase, namely  $B'(T) = |B'| e^{i\vartheta(T')}$  and  $\check{\eta}'_{p1} = |\check{\eta}'_{p1}| e^{i\vartheta_\eta}$ , the coefficients  $d_n$  are then given by

$$d_n = \frac{\Omega}{4\pi} \int_{-2\pi/\Omega}^{2\pi/\Omega} \tanh\left(\frac{\hat{\alpha}}{\epsilon} \Omega |B'| |\check{\eta}'_{p1}|_{y'=b/2} \cos\psi\right) e^{-in\Omega t'/2} dt', \quad (\text{B } 12)$$

where the variable  $\psi$  is defined as  $\psi = \Omega t'/2 + kx' + \pi/2 + \vartheta(T') + \vartheta_\eta|_{y'=b/2}$ . Since the rescaled steepness coefficient  $\hat{\alpha}/\epsilon$  is large enough, the hyperbolic tangent can be expanded as the sum of the sign function plus a small correction  $f(\epsilon, \psi)$ , which satisfies  $\int_{-2\pi}^{2\pi} f(\epsilon, \psi) e^{-in\Omega t'/2} d\psi = O(\epsilon)$ . Hence, equation (B 12) is expanded as

$$\begin{aligned} d_n &= \frac{\Omega}{4\pi} \int_{-2\pi/\Omega}^{2\pi/\Omega} \text{sgn}\left(\frac{\hat{\alpha}}{\epsilon} \Omega |B'| |\check{\eta}'_{p1}|_{y'=b/2} \cos\psi\right) e^{-in\Omega t'/2} dt' + O(\epsilon) \\ &= e^{in(kx' + \pi/2 + \vartheta(T') + \vartheta_\eta|_{y'=b/2})} \frac{1}{2\pi} \int_{-\pi}^{\pi} \text{sgn}(\cos\psi) e^{-in\psi} d\psi + O(\epsilon) \\ &= \frac{2}{\pi} c_n e^{in(kx' + \pi/2 + \vartheta(T') + \vartheta_\eta|_{y'=b/2})} + O(\epsilon). \end{aligned} \quad (\text{B } 13)$$

When  $n = 1$ , the Fourier coefficient  $c_1$  in (B 13) reads

$$\frac{2}{\pi} c_1 = \frac{1}{2\pi} \int_{-\pi}^{\pi} \text{sgn}(\cos\psi) e^{-i\psi} d\psi = \frac{2}{\pi}, \quad (\text{B } 14)$$

which means  $c_1 = 1$ . Since the stability analysis focuses exclusively on the fundamental subharmonic mode, we approximate the tangent function (B 11) by its leading-order Fourier expansion term, which reads

$$\tanh\left(\frac{\hat{\alpha}}{\epsilon} \frac{\partial \eta'_{p1}}{\partial t'} \bigg|_{y'=b/2}\right) = \frac{2}{\pi} e^{i(\Omega t'/2 + kx' + \pi/2 + \vartheta(T') + \vartheta_\eta|_{y'=b/2})} + \text{c.c.} \quad (\text{B } 15)$$

Substituting (B 15) into the expression of  $\theta_{p2}$  (3.13) and the contact line condition (3.12c), one obtains

$$\frac{\partial \check{\eta}'_{p2}}{\partial y'} = -\frac{i\hat{\alpha}}{\pi \sin^2 \theta_s} \frac{\check{\eta}'_{p1}}{|\check{\eta}'_{p1}|} \frac{B'}{|B'|}, \quad \text{at } y' = \frac{b}{2}. \quad (\text{B } 16)$$

This condition gives a nonlinear correction to the previous order, which reflects the fast variation of contact angle in the hysteresis range at small contact line velocity. Because the  $\text{sgn}$  function is utilized to approximate the hyperbolic tangent, (B 16) only depends on the phase of the velocity. As the free surface fluctuates up-and-down, the contact line condition provides a different correction, which is consistent with the periodic feature of Faraday waves, and cannot be incorporated by the linear Hamraoui's model (3.3).

Substituting (B 16) into the solvability condition (B 10), an amplitude equation is obtained, leading to (3.15).

## Appendix C. Image analysis and extraction of the dynamic contact angle

In § 4.1, an image analysis program implemented in MATLAB is developed to automatically extract contact angle values from sequential video frame by frame. This image processing procedure is inspired by the contact angle measurement techniques developed by Kalantarian *et al.* (2011) and Shen *et al.* (2024) for droplets on flat substrates. The details are described as follows:

- (i) For each frame, the snapshot is first cropped to mainly contain the meniscus region and adjacent lateral walls, followed by the employment of a Gaussian filter with a standard deviation of 3 to reduce high-frequency noise. Subsequently, the meniscus boundary is extracted using the Canny edge detector with a threshold of 0.23, which provides robust feature extraction.
- (ii) We then identify the positions of two lateral walls. Taking advantage of the symmetry between the meniscus and its reflection, the lateral walls act as the axis of symmetry. Their horizontal positions are therefore determined by averaging the horizontal coordinates of a set of symmetric midpoints identified at different levels. To rigorously validate the accuracy of this step, the calculated gap size is compared with the known physical value of 4.8 mm.
- (iii) From the free surface pixel coordinates (a data set with 265 or more valid values) acquired between the identified lateral boundaries, a subset of 260 points is used to construct a sixth-order polynomial

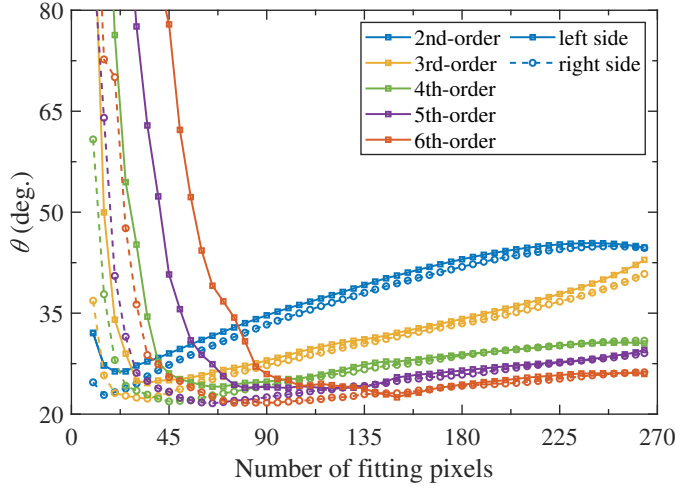


Figure 17. Comparison of the fitted contact angle  $\theta$  for varying numbers of pixels and different order of polynomials. Polynomial fits from second-order to sixth-order are tested. Solid lines with squares denote the results of the contact angle on the left lateral wall, while dashed lines with circles denote those on the right lateral wall.

representation of the meniscus profile, namely  $\eta'(y') = \sum_{n=0}^6 a_n y'^n$ . The contact angle is calculated from the derivative of the fitted polynomial at the lateral wall positions, using the formulation:

$$\theta_l = \frac{\pi}{2} + \arctan \left. \frac{d\eta'}{dy'} \right|_{y'=-b/2}, \quad \theta_r = \frac{\pi}{2} - \arctan \left. \frac{d\eta'}{dy'} \right|_{y'=b/2}. \quad (\text{C } 1)$$

Finally, we take the average of the contact angles on the two lateral walls as the final values, that is  $\theta = (\theta_l + \theta_r)/2$ .

The optimal polynomial order and number of pixels for the fitting procedure are determined following the method employed by Shen *et al.* (2024). Figure 17 presents a comparison of the calculated contact angle with various polynomial orders (second to sixth order) and pixel numbers (10 to 265 points). Higher-order polynomial fits show faster convergence to stable values, while simultaneously improving the agreement between measurements obtained from opposite sidewalls. The sixth-order polynomial demonstrates the optimal convergence characteristics, exhibiting stability when approximately 240 ~ 260 fitting pixels are employed. This formulation is consequently adopted as the preferred fitting strategy.

#### REFERENCES

- ALARCÓN, HÉCTOR, HERRERA-MUÑOZ, MATÍAS, PÉRINET, NICOLAS, MUJICA, NICOLÁS, GUTIÉRREZ, PABLO & GORDILLO, LEONARDO 2020 Faraday-wave contact-line shear gradient induces streaming and tracer self-organization: From vortical to hedgehoglike patterns. *Physical Review Letters* **125** (25), 254505.
- ARNOLD, CRAIG B, SERRA, PERE & PIQUÉ, ALBERTO 2007 Laser direct-write techniques for printing of complex materials. *Mrs Bulletin* **32** (1), 23–31.
- BENJAMIN, THOMAS BROOKE & URSELL, FRITZ JOSEPH 1954 The stability of the plane free surface of a liquid in vertical periodic motion. *Proceedings of the Royal Society of London. Series A*. **225** (1163), 505–515.
- BEYER, J & FRIEDRICH, R 1995 Faraday instability: linear analysis for viscous fluids. *Physical Review E* **51** (2), 1162.
- BONGARZONE, ALESSANDRO, JOURON, BAPTISTE, VIOLA, FRANCESCO & GALLAIRE, FRANÇOIS 2023 A revised gap-averaged floquet analysis of faraday waves in hele-shaw cells. *Journal of Fluid Mechanics* **977**, A45.
- CHEN, PU, LUO, ZHENGYUAN, GÜVEN, SINAN, TASOGLU, SAVAS, GANESAN, ADARSH VENKATARAMAN, WENG, ANDREW & DEMIRCI, UTKAN 2014 Microscale assembly directed by liquid-based template. *Advanced materials (Deerfield Beach, Fla.)* **26** (34), 5936.
- CHEN, PEILONG & VINALS, JORGE 1999 Amplitude equation and pattern selection in faraday waves. *Physical Review E* **60** (1), 559.
- COCCIARO, BRUNO, FAETTI, SANDRO & FESTA, CRESCENZO 1993 Experimental investigation of capillarity effects on surface gravity waves: non-wetting boundary conditions. *Journal of Fluid Mechanics* **246**, 43–66.

- COLVILLE, STUART WILLIAM, SCOLAN, Y-M, GAMBIOLI, FRANCESCO, GREAVES, DEBORAH, RANSLEY, EDWARD & LEE, YEAW CHU 2025 Faraday waves and period tripling in a horizontal circular tank. *Journal of Fluid Mechanics* **1006**, A4.
- DE GENNES, PIERRE-GILLES 1985 Wetting: statics and dynamics. *Reviews of modern physics* **57** (3), 827.
- DOUADY, S & FAUVE, S 1988 Pattern selection in faraday instability. *Europhysics letters* **6** (3), 221.
- EDWARDS, W STUART & FAUVE, S 1994 Patterns and quasi-patterns in the faraday experiment. *Journal of Fluid Mechanics* **278**, 123–148.
- FALTINSEN, OM 2017 Sloshing. *Advances in Mechanics* **47** (1), 201701.
- FARADAY, MICHAEL 1831 On a peculiar class of acoustical figures; and on certain forms assumed by groups of particles upon vibrating elastic surfaces. *Philosophical transactions of the Royal Society of London* **121**, 299–340.
- GONDRET, PHILIPPE & RABAUD, MARC 1997 Shear instability of two-fluid parallel flow in a hele–shaw cell. *Physics of Fluids* **9** (11), 3267–3274.
- GOOD, ROBERT J 1992 Contact angle, wetting, and adhesion: a critical review. *Journal of adhesion science and technology* **6** (12), 1269–1302.
- HAMRAOUI, AHMED, THURESSON, KRISTER, NYLANDER, TOMMY & YAMINSKY, VASSILI 2000 Can a dynamic contact angle be understood in terms of a friction coefficient? *Journal of colloid and interface science* **226** (2), 199–204.
- HOCKING, LM 1987 The damping of capillary–gravity waves at a rigid boundary. *Journal of fluid mechanics* **179**, 253–266.
- JIANG, LEI, PERLIN, MARC & SCHULTZ, WILLIAM W 2004 Contact-line dynamics and damping for oscillating free surface flows. *Physics of Fluids* **16** (3), 748–758.
- KALANTARIAN, A, DAVID, R, CHEN, J & NEUMANN, AW 2011 Simultaneous measurement of contact angle and surface tension using axisymmetric drop-shape analysis-no apex (adsa-na). *Langmuir* **27** (7), 3485–3495.
- KEULEGAN, GARBIS H 1959 Energy dissipation in standing waves in rectangular basins. *Journal of Fluid Mechanics* **6** (1), 33–50.
- KHATTAB, IBRAHIM SADEK, BANDARKAR, FARZANA, FAKHREE, MOHAMMAD AMIN ABOLGHASSEMI & JOUYBAN, ABOLGHASEM 2012 Density, viscosity, and surface tension of water+ ethanol mixtures from 293 to 323k. *Korean Journal of Chemical Engineering* **29**, 812–817.
- KIDAMBI, R 2009 Capillary damping of inviscid surface waves in a circular cylinder. *Journal of fluid mechanics* **627**, 323–340.
- KUMAR, KRISHNA & TUCKERMAN, LAURETTE S 1994 Parametric instability of the interface between two fluids. *Journal of Fluid Mechanics* **279**, 49–68.
- LI, JING, LI, XIAOCHEN, CHEN, KAIJIE, XIE, BIN & LIAO, SHIJUN 2018a Faraday waves in a hele–shaw cell. *Physics of Fluids* **30** (4).
- LI, JING, LI, XIAOCHEN & LIAO, SHIJUN 2019a Stability and hysteresis of faraday waves in hele–shaw cells. *Journal of Fluid Mechanics* **871**, 694–716.
- LI, XINGSHENG & LI, JING 2024 The stability analysis based on viscous theory of faraday waves in hele–shaw cells. *Physics of Fluids* **36** (3).
- LI, XIAOCHEN, LI, JING, LI, XIAOMING, LIAO, SHIJUN & CHEN, CHAOHE 2019b Effect of width on the properties of faraday waves in hele–shaw cells. *Science China Physics, Mechanics & Astronomy* **62**, 1–6.
- LI, XIAOCHEN, LI, XIAOMING & LIAO, SHIJUN 2018b Observation of two coupled faraday waves in a vertically vibrating hele–shaw cell with one of them oscillating horizontally. *Physics of Fluids* **30** (1).
- LIU, FUSHUI, KANG, NING, LI, YIKAI & WU, QING 2019 Experimental investigation on the atomization of a spherical droplet induced by faraday instability. *Experimental Thermal and Fluid Science* **100**, 311–318.
- MILES, JOHN W 1967 Surface-wave damping in closed basins. *Proceedings of the Royal Society of London. Series A*. **297** (1451), 459–475.
- MILNER, SCOTT THOMAS 1991 Square patterns and secondary instabilities in driven capillary waves. *Journal of fluid mechanics* **225**, 81–100.
- MONSALVE, EDUARDO, MAUREL, AGNÈS, PAGNEUX, VINCENT & PETITJEANS, PHILIPPE 2022 Space-time-resolved measurements of the effect of pinned contact line on the dispersion relation of water waves. *Physical Review Fluids* **7** (1), 014802.
- MÜLLER, HANNS WALTER 1993 Periodic triangular patterns in the faraday experiment. *Physical review letters* **71** (20), 3287.
- NAYFEH, ALI H 1993 *Introduction to perturbation techniques*. Wiley.
- NOBLIN, X, BUGUIN, A & BROCHARD-WYART, F 2004 Vibrated sessile drops: Transition between pinned and mobile contact line oscillations. *The European Physical Journal E* **14**, 395–404.
- PÉRINET, NICOLAS, GUTIÉRREZ, PABLO, URRÁ, HÉCTOR, MUJICA, NICOLÁS & GORDILLO, LEONARDO 2017 Streaming patterns in faraday waves. *Journal of Fluid Mechanics* **819**, 285–310.

- PÉRINET, NICOLAS, JURIC, DAMIR & TUCKERMAN, LAURETTE S 2009 Numerical simulation of faraday waves. *Journal of Fluid Mechanics* **635**, 1–26.
- POPINET, STÉPHANE 2003 Gerris: a tree-based adaptive solver for the incompressible euler equations in complex geometries. *Journal of computational physics* **190** (2), 572–600.
- POPINET, STÉPHANE 2009 An accurate adaptive solver for surface-tension-driven interfacial flows. *Journal of Computational Physics* **228** (16), 5838–5866.
- PRADENAS, BASTIÁN, ARAYA, ISIDORA, CLERC, MARCEL G, FALCÓN, CLAUDIO, GANDHI, PUNIT & KNOBLOCH, EDGAR 2017 Slanted snaking of localized faraday waves. *Physical Review Fluids* **2** (6), 064401.
- RACHIK, AZEDDINE & ANISS, SAÏD 2023 Effects of finite depth and surface tension on the linear and weakly non-linear stability of faraday waves in hele-shaw cell. *Fluid Dynamics Research* **55** (4), 045506.
- RAJCHENBACH, JEAN & CLAMOND, DIDIER 2015 Faraday waves: their dispersion relation, nature of bifurcation and wavenumber selection revisited. *Journal of Fluid Mechanics* **777**, R2.
- RAJCHENBACH, JEAN, LEROUX, ALPHONSE & CLAMOND, DIDIER 2011 New standing solitary waves in water. *Physical review letters* **107** (2), 024502.
- SAN, OMER & STAPLES, ANNE E 2012 An improved model for reduced-order physiological fluid flows. *Journal of Mechanics in Medicine and Biology* **12** (03), 1250052.
- SCHWARTZ, LEONARD 1986 Stability of hele–shaw flows: The wetting-layer effect. *The Physics of fluids* **29** (9), 3086–3088.
- SHAO, X, GABBARD, CT, BOSTWICK, JB & SAYLOR, JR 2021a On the role of meniscus geometry in capillary wave generation. *Experiments in Fluids* **62**, 1–4.
- SHAO, X, WILSON, P, SAYLOR, JR & BOSTWICK, JB 2021b Surface wave pattern formation in a cylindrical container. *Journal of Fluid Mechanics* **915**, A19.
- SHEN, JIAXING, LEE, YAERIM, LI, YUANZHE, ZALESKI, STÉPHANE, AMBERG, GUSTAV & SHIOMI, JUNICHIRO 2024 Dynamic hysteresis of an oscillatory contact line. *Journal of Fluid Mechanics* **1000**, A34.
- TING, CHAO-LUNG & PERLIN, MARC 1995 Boundary conditions in the vicinity of the contact line at a vertically oscillating upright plate: an experimental investigation. *Journal of Fluid Mechanics* **295**, 263–300.
- TURKOZ, EMRE, KANG, SEUNGYEON, DU, XIAOHAN, DEIKE, LUC & ARNOLD, CRAIG B 2019 Reduction of transfer threshold energy for laser-induced jetting of liquids using faraday waves. *Physical Review Applied* **11** (5), 054022.
- VIOLA, FRANCESCO, ARRATIA, CRISTOBAL & GALLAIRE, FRANÇOIS 2016 Mode selection in trailing vortices: harmonic response of the non-parallel batchelor vortex. *Journal of Fluid Mechanics* **790**, 523–552.
- VIOLA, FRANCESCO, BRUN, P-T & GALLAIRE, FRANÇOIS 2018 Capillary hysteresis in sloshing dynamics: a weakly nonlinear analysis. *Journal of Fluid Mechanics* **837**, 788–818.
- VIOLA, FRANCESCO, GALLAIRE, FRANÇOIS & DOLLET, BENJAMIN 2017 Sloshing in a hele-shaw cell: experiments and theory. *Journal of Fluid Mechanics* **831**, R1.
- WESTRA, MARK-TIELE, BINKS, DOUG J & VAN DE WATER, WILLEM 2003 Patterns of faraday waves. *Journal of Fluid Mechanics* **496**, 1–32.
- WILSON, P, SHAO, X, SAYLOR, JR & BOSTWICK, JB 2022 Role of edge effects and fluid depth in azimuthal faraday waves. *Physical Review Fluids* **7** (1), 014803.
- WOMERSLEY, JOHN R 1955 Method for the calculation of velocity, rate of flow and viscous drag in arteries when the pressure gradient is known. *The Journal of physiology* **127** (3), 553.
- YANG, XIAOTAO, ZHENG, JIA, LUO, XIANFENG, XIAO, HONGYAN, LI, PEIJIA, LUO, XIAODONG, TIAN, YE, JIANG, LEI & ZHAO, DONG 2024 Ethanol-water clusters determine the critical concentration of alcoholic beverages. *Matter* **7** (5), 1724–1735.
- ZHANG, WENBIN & VIÑALS, JORGE 1997 Pattern formation in weakly damped parametric surface waves. *Journal of Fluid Mechanics* **336**, 301–330.